Radiance Simulations in Support of Climate Services

Paul Poli, Rob Roebeling, Viju Oommen John, Marie Doutriaux-Boucher, Joerg Schulz, Alessio Lattanzio, Kristina Petraityte, Mike Grant, Timo Hanschmann, Jacobus Onderwaater, et al.

Radiance Simulations in Support of Climate Services

Paul Poli[1], Rob Roebeling[2], Viju Oommen John[2], Marie Doutriaux-Boucher[2], Joerg Schulz[2], Alessio Lattanzio[2], Kristina Petraityte[2], Mike Grant[2], Timo Hanschmann[2], Jacobus Onderwaater[2], Oliver Sus[2], Roger Huckle[2], Dorothee Coppens[2], Bertrand Théodore[2], Thomas August[2], Adrian John Simmons[1], William Bell[1], Jonathan Mittaz[3], Thomas Hall[4], Jerome Vidot[5], Pascal Brunel[6], James E. Johnson[7], Emily B. Zamkoff[8], Atheer F. Al-Jazrawi[8], Asghar E. Esfandiari[7], Irina V. Gerasimov[7], and Shinya Kobayashi[9]

[1]ECMWF
[2]EUMETSAT
[3]University of Reading
[4]SPASCIA
[5]Meteo-France
[6]Meteo-France (retired)
[7]NASA Goddard Space Flight Center (GSFC) Goddard Earth Sciences Data and Information Services Center (GES DISC) and ADNET Systems, Inc.
[8]NASA Goddard Space Flight Center (GSFC) Goddard Earth Sciences Data and Information Services Center (GES DISC) and Telophase Corporation
[9]Japan Meteorological Agency

June 21, 2023

Radiance Simulations in Support of Climate Services

P. Poli[1]*†, R. Roebeling[2], V. O. John[2], M. Doutriaux-Boucher[2], J. Schulz[2], A. Lattanzio[2], K. Petraityte[2], M. Grant[2], T. Hanschmann[2], J. Onderwaater[2], O. Sus[2], R. Huckle[2], D. Coppens[2], B. Theodore[2], T. August[2], A. J. Simmons[1], B. Bell[1], J. Mittaz[3], T. Hall[4]‡, J. Vidot[5], P. Brunel[5+], J. E. Johnson[6,7], E. B. Zamkoff[6,8], A. F. Al-Jazrawi[6,8], A. E. Esfandiari[6,7], I. V. Gerasimov[6,7], S. Kobayashi[9]

[1] European Centre for Medium-Range Weather Forecasts (ECMWF), Bonn, Germany.

[2] European Organisation for the Exploitation of Meteorological Satellites (EUMETSAT), Darmstadt, Germany.

[3] University of Reading, United Kingdom.

[4] Space Science & Algorithmics (SPASCIA), Ramonville Saint-Agne, France.

[5] CNRM, Université de Toulouse, Météo-France, CNRS, Lannion, France.

[6] NASA Goddard Space Flight Center (GSFC), Goddard Earth Sciences Data and Information Services Center (GES DISC), Greenbelt, Maryland, USA.

[7] ADNET Systems, Inc., Bethesda, Maryland, USA.

[8] Telophase Corporation, Greenbelt, Maryland, USA.

[9] Japan Meteorological Agency (JMA), Tokyo, Japan.

* Corresponding author**:** Paul Poli (paul.poli@ecmwf.int)

† Previously at EUMETSAT.

‡ Previously at University of Reading.

+ Retired.

Key Points:

- Radiance simulations can help characterize two essential inputs of climate services, satellite data records and reanalyses
- Uncertainties in observations collected by the Spektrometer Interferometer-1 flown on a Soviet satellite in 1979 were estimated
- Radiance simulations of satellite instruments can provide information on the quality and realism of climate reanalyses

Abstract

Climate services are largely supported by climate reanalyses and by satellite Fundamental (Climate) Data Records (F(C)DRs). This paper demonstrates how the development and the uptake of F(C)DR benefit from radiance simulations, using reanalyses and radiative transfer models. We identify three classes of applications, with examples for each application class. The first application is to validate assumptions during F(C)DR development. Hereto we show the value of applying advanced quality controls to geostationary European (Meteosat) images. We also show the value of a cloud mask to study the spatio-temporal coherence of the impact of the Mount Pinatubo volcanic eruption between Advanced Very High Resolution Radiometer (AVHRR) and the High-resolution Infrared Radiation Sounder (HIRS) data. The second application is to assess the coherence between reanalyses and observations. Hereto we show the capability of reanalyses to reconstruct spectra observed by the Spektrometer Interferometer (SI-1) flown on a Soviet satellite in 1979. We also present a first attempt to estimate the random uncertainties from this instrument. Finally, we investigate how advanced bias correction can help to improve the coherence between reanalysis and Nimbus-3 Medium-Resolution Infrared Radiometer (MRIR) in 1969. The third application is to inform F(C)DR users about particular quality aspects. We show how simulations can help to make a better-informed use of the corresponding F(C)DR, taking as examples the Nimbus-7 Scanning Multichannel Microwave Radiometer (SMMR), the Meteosat Second Generation imager, and the DMSP Special Sensor Microwave Water Vapor Profiler (SSM/T-2).

1 Introduction

Recognizing increased inter-relations between human activities, impacts, and evolving climate phenomena, the World Climate Conference-3 (WCC-3, 2009a) fostered a substantial expansion and enhancement of climate services worldwide. Although several World Meteorological Organization (WMO) members already operated climate services before 2009, this conference was a milestone in the establishment of the Global Framework for Climate Services (GFCS). In coordination with several other organizations, including the United Nations Educational, Scientific and Cultural Organization (UNESCO), the United Nations Environment Programme (UNEP), the Food and Agriculture Organization of the United Nations (FAO), and the International Council for Science (ICSU), the GFCS was established to complement and support the work of the Intergovernmental Panel on Climate Change (IPCC) and the United Nations Framework Convention on Climate Change (UNFCCC) (WCC-3, 2009b).

More than ten years later, climate services have evolved beyond the scope of classical climatology. Moving on from the classical form of climate means, compiled and served to the public by national weather agencies, climate activities today embrace a bundle of relationships and exchanges between the climate data and actors and societal applications (e.g., Brasseur & Gallardo, 2016). Furthermore, environmental observations are no longer the exclusive remit of selected public agencies: observations are now collected, assembled, curated, and served by a variety of actors including, e.g., space agencies, universities, research programs and organizations involved in environmental monitoring, but also associative or private initiatives, and structural elements such as cloud-computing platforms (e.g., Thorpe & Rogers, 2018). These actors operate alongside traditional national weather agencies that remain, in most cases, ultimately responsible for key properties of climate data record monitoring (Mahon et al., 2019).

Climate monitoring is only one component of climate services (World Meteorological Organization (WMO), 2018). Other components, of which some of them are related to monitoring, include climate reanalyses, climate indicators and indices, longer-term forecast elements that include predictions and projections, and attribution of climate phenomena. This last component is crucial to understand the causes of, and later better project or predict, selected climate phenomena and their impacts, and develop relevant mitigation or adaptation measures. Enabled by methods such as developed by Hasselmann (1997), attribution is a preliminary step before further climate adaptation or mitigation measures may be taken. Attribution is also called to play a role in the UNFCCC Warsaw International Mechanism (WIM) to deal with loss and damage due to climate change (Parker et al., 2015). Beyond this, without an underlying understanding of the causes of important climate phenomena (such as 'extremes') and their inter-relations with human activities, the risks run high of counter-productive societal measures that can worsen the issues at stake (e.g., Schipper, 2020).

Even if climate services are not limited to climate monitoring and the corresponding preparation and provision of observation-based Climate Data Records (CDRs), these data records remain the necessary physical basis for all other components of the climate services. As such, observation-based products underpin the outcomes of IPCC's First Working Group that examines the physical science of climate change (Masson-Delmotte et al., 2021). Similarly, observations are often depicted at the onset of the weather and climate value chain (e.g., Ruti et al., 2020).

The present paper focuses on a method to accelerate the development and uptake of satellite-based CDRs. These are optimally based on satellite sensor data in the form of Fundamental Climate Data Records (FCDRs), or else on Fundamental Data Records (FDRs), also referred to as Sensor Data Records (SDRs) (Privette et al., 2023). Hereafter we evaluate the quality of F(C)DRs by comparing them with simulated observations. While the use of simulations to survey the quality of satellite-based observations and products over the long-term is not a novelty (e.g., Jackson & Soden, 2007; Newman et al., 2020), their use to support the CDR development is rather recent.

The outline of this paper is as follows. Section 2 presents the data and methodology. Sections 3 to 5 showcase three different classes of applications, namely, Class-I: validating assumptions (section 3), Class-II: assessing coherence between observations and reanalyses (section 4), and Class-III: informing users (section 5). Section 6 discusses the results. Finally, section 7 presents conclusions and prospects for future work.

2 Data and methodology

Satellite observations considered in this paper come from several instruments. The radiative transfer simulations use reanalysis fields as input, and provide in return brightness temperatures (or reflectances), for microwave channels and visible, near-infrared, shortwave infrared, and thermal infrared channels. The differences between the observations and simulations are hereafter called departures. The methods and data used in the paper are presented below.

2.1 Radiative transfer simulations

Since the early days of satellite meteorology, the accurate and faithful numerical simulation of satellite measurements has been a topic of research and active development (e.g.,

Gordon, 1962). From early on, the simulation methods for radiative transfer have involved a mix of exact solutions and numerical methods (e.g., Hunt & Grant, 1969; Rodgers & Walshaw, 1963). A representation of the so-called direct (or forward) model is an essential tool to exploit the measurements and map the signals into useful information (e.g., Rodgers, 1990). Also, by allowing physical quantities to be estimated from the measurements, such as inversion or retrieval process (e.g., Stephens, 1994), any improvement to the forward models further helps to enhance the understanding of the observed natural phenomena (e.g., Houborg & McCabe, 2016).

Simulations of satellite observations have proven to bring about additional benefits, in line with the continuous development in Earth sciences. This is an iterative process where the lessons learnt from the confrontation of simulation results with actual observations enhance our understanding of important effects affecting the quality the observations, thereby allowing to repeat the data processing or simulations with improved algorithms, or to improve future instrument design. This was shown, in particular, for the physical interactions between the observed phenomena and the measurement process (e.g., Bell et al., 2010; John & Buehler, 2004; Joiner & Poli, 2005). These iterative improvements enable researchers to continue extracting ever-increasing value from these observations for societal applications, such as Numerical Weather Prediction (NWP) (e.g., Shahabadi et al., 2018). Furthermore, such enhanced understanding also helps to refine the design of new-generation instruments or data records. This allows, for example, better understanding instrument ageing processes (e.g., Munro et al., 2016; Quast et al., 2019), detecting the impact of imperfections that were previously thought negligible (e.g., Lu & Bell, 2014), or releasing new versions of the data records that correct for observation sampling effects (e.g., Mears & Wentz, 2017). Another benefit is to enhance our understanding of discrepancies between models and observations, especially for data assimilation, whose remit is to exploit these differences to extract information, even when a bias correction procedure is necessary (e.g., Joiner & Rokke, 2000). On longer timescales, quantifying discrepancies between models and observations can also help pinpoint effects that are important to consider in models, such as anthropogenic effects (e.g., De Vrese & Hagemann, 2018).

Alongside all these applications sits also research towards using novel technology instruments (e.g., Doutriaux-Boucher et al., 1998) or to revisit early satellite data records (e.g., Poli et al., 2017). However, climate research presents several distinct challenges when it comes to observation data simulators. First, the time-series covered by climate model and by related satellite-based CDR products are necessarily long. This makes running a full data assimilation system (with underpinning Earth-system models and covering many observation types) an overly computationally-expensive and inadequate venture. This is also partly unnecessary in the face of the efforts already deployed by large modelling centres to create model-gridded global decadal datasets, such as reanalyses, which gradually widen their remits to exploit (and hence simulate) an increasing diversity of satellite-based data records. Secondly, the variety of observation data that are available exceeds the variety of data encountered in a single data assimilation window that covers a few hours of a given date. Furthermore, a thorough and relevant assessment of reprocessed satellite data mandates to use state-of-the-art simulators that can be applied to the latest versions of the data records quickly. This timing is not compatible with the planning of reanalyses productions, which take years to prepare and execute. Finally, such assessments require efficient and traceable simulation tools, while maintaining a strong link to community-driven efforts that continually improve such simulation tools, based on the latest science (e.g., Swales et al., 2018).

Owing to these specificities, data simulators can be beneficial in at least three different points of the climate value chain. The first possibility is to use them during the F(C)DR development phase, to validate the assumptions made. A second possibility is to use them after the production of a F(C)DR, but before data release, to assess the realism and coherence between a new F(C)DR and state-of-the-art Earth system reanalyses. A third possibility is post-production, even possibly after a F(C)DR release, to inform the data users about likely sources of variability present in the data (e.g., natural variability versus instrumental or sampling artefacts). These represent many feed-back opportunities. Note this paper does not discuss the issue of using simulators as integral part of the F(C)DR production chain.

All these potential benefits have contributed to the development of a standalone RADiance SIMulator (RADSIM) (Hocking, 2022), able to simulate all the satellite sensors supported by the Radiative Transfer for Television Infrared Orbiting Satellite (TIROS) Operational Vertical Sounder (TOVS) (RTTOV, Saunders et al., 2018). It must be recalled that both elements, RADSIM and RTTOV, benefit from a long-term support of the EUMETSAT climate services and development plan, with activities distributed between the EUMETSAT central facility and its Satellite Applications Facility (SAF) network, including the NWP-SAF, for these simulators. The results shown in this manuscript build on an implementation of RADSIM and RTTOV in the EUMETSAT infrastructure, with massively parallel computations carried out on a multi-node cluster computing system.

In the present study, we use RADSIM interfaced with RTTOV version 13.0, except for simulating data from the Medium-Resolution Infrared Radiometer (MRIR) where we used RTTOV version 12.2. Additional details about the radiance simulation configuration are given in Supplement Text S1.

2.2 Reanalysis data

Reanalyses are used for their ability to provide temporally and spatially complete fields of key atmospheric properties. Several global comprehensive reanalyses of the atmosphere have been produced in the recent past. The following are considered in the present work, cited in the order they were released: ERA-Interim (Dee et al., 2011; ECMWF, 2009), JRA-55 (Shinya Kobayashi et al., 2015; Japan Meteorological Agency, 2013), ERA-20C (Poli et al., 2016; ECMWF, 2014), ERA5 (Hersbach et al., 2020; Copernicus Climate Change Service, 2018), and JRA-3Q (S. Kobayashi et al., 2021; Japan Meteorological Agency, 2022). Among these, only ERA5 provides hourly analyses. For all others, the radiative transfer simulator uses 6-hourly analyses. The reanalyses are used at 0.5° x 0.5° (latitude, longitude) horizontal resolution, except for MRIR simulations that used ERA5 data at 1°x1° resolution. The geophysical parameters include temperature, humidity, and ozone (for all available model levels), as well as near-surface wind speed, temperature, and humidity, and surface air pressure, surface geopotential, skin temperature, land-sea mask, and sea-ice cover. The reanalysis cloud and precipitation information is not used in the simulations.

2.3 Satellite data

This work uses data records from 8 different satellite instruments:

- Meteosat Visible Infra-Red Imager (MVIRI), flown on Meteosat First Generation (MFG) satellites, Meteosat-2 to -7 (EUMETSAT, 2020),

- Spinning Enhanced Visible and InfraRed Imager (SEVIRI), flown on Meteosat Second Generation (MSG) satellites, Meteosat-8 to -11 (EUMETSAT, 2015)
- Medium-Resolution Infrared Radiometer (MRIR), flown on several TIROS and Nimbus satellites, noting that this study only uses data collected by Nimbus-3 (McCulloch, 2014),
- Spektrometer Interferometer (SI-1), flown on Soviet weather satellites Meteor-28 and -29, noting that this study only uses data collected by Meteor-29 (Poli et al., 2023),
- High-resolution Infrared Radiation Sounder (HIRS), flown on NOAA Polar Operational Environmental Satellites (POES) TIROS/N, NOAA-6 to -19 and EUMETSAT polar-orbiting satellites, Metop-A and -B (EUMETSAT, 2022),
- Advanced Very High Resolution Radiometer (AVHRR) flown on the same satellites as HIRS as well as Metop-C (EUMETSAT, 2023),
- Scanning Multichannel Microwave Radiometer (SMMR), flown on satellites Seasat and Nimbus-7, noting that this study only uses data collected by Nimbus-7 (Fennig et al., 2017),
- Special Sensor Microwave Water Vapor Profiler (SSM/T-2), flown on U.S. DMSP satellites F-11, -12, -14, and -15 (EUMETSAT, 2021).

The first 2 instruments are visible and infrared imagers on geostationary satellites, the next 4 are visible and/or infrared imagers or infrared sounders on polar-orbiting satellites, and the last 2 are microwave radiometers on polar-orbiting satellites. Several instruments are historical sensors, given their early data record.

While it would take too long to expand all details of these instruments, as well as their detailed configurations, Table 1 provides a summary of some of their key characteristics. Other references, such as the WMO Observing Systems Capability Analysis and Review tool (OSCAR) Space database (https://space.oscar.wmo.int), provide further information for these instruments. Additional instrument information is given later, as relevant, when presenting the simulation applications.

Table 1 indicates if the data records have been used in one way or another in global reanalysis, indicating here the situation only for the data sources assimilated in ERA5 (Hersbach et al., 2020), because it is the only reanalysis used for all comparisons. There are several cases of indirect data use in ERA5, as indicated in Table 1. There are only three cases of direct assimilation of the radiance data considered in the present study into ERA5 (Hersbach et al., 2020): (1) MVIRI after 2001, (2) SEVIRI, and (3) HIRS.

Sensor	Years of operation	IFOV size[b]	Scanning pattern	Nb. of channels (wavelengths or frequencies)	DOI[c]
MVIRI [a] *	1977-2017	4.5 km	Earth disc, every 30 minutes	2 (6.4, 11.5 μm) [d]	10.15770/EUM_SEC_CLM_0009
SEVIRI [a] * +	2002-2023	3 km	Earth disc, every 15 minutes	8 (3.9—13.4 μm) [d]	10.15770/EUM_SEC_CLM_0008
MRIR [a] §	1969-1970	55 km	85 pixels along 3000 km swath	4 (6.5—23 μm) [d]	10.5067/XTJ53AK84QRL
SI-1 [a]	1977, 1979	25 km	Nadir only, every 100 km along-track	579 (6—25 μm)	10.15770/EUM_SEC_CLM_0086 [e]
HIRS [a] +	1978-2023	20 km [f]	56 pixels along 2200 km swath	19 (3.7—15 μm) [d]	10.15770/EUM_SEC_CLM_0026
AVHRR [a] *	1978-2023	1.1 km [g]	2048 pixels [g] along 2900 km swath	AVHRR/1: 4 (0.6—11 μm), AVHRR/2: 5 (0.6—12 m), AVHRR/3: 6 (idem)	10.15770/EUM_SEC_CLM_0060
SMMR [a] *	1978-1987	20—120 km	94 pixels along 780 km swath	10 (6.6—37 GHz)	10.5676/EUM_SAF_CM/FCDR_MWI/V003
SSM/T-2 [a]	1994-2005	48 km	28 pixels along 1500 km swath	5 (91—183 GHz)	10.15770/EUM_SEC_CLM_0050

Table 1. Overview of selected characteristics for instruments considered in the present study. Several instruments still operate at the time of writing. +Radiance data from this instrument were assimilated in ERA5. *Radiance data from this instrument were indirectly used in ERA5, as follows, *via* assimilation of atmospheric motion vector (MVIRI, SEVIRI, AVHRR), or as input to the sea-surface temperature forcing (AVHRR) or the sea-ice forcing (SMMR). §The information given here pertains only to Nimbus-3. [a]More information about this instrument is accessible from WMO OSCAR at https://space.oscar.wmo.int. [b]Instantaneous Field-Of-View (IFOV), at the sub-satellite point. [c]Digital Object Identifier (DOI) for the data used in the present work, accessible at https://doi.org/<DOI>. [d]Visible channels from this instrument are not simulated in the present work. [e]This is the DOI reserved for future publication of the entire data record, noting that the subset of data used in the present work are available from DOI:10.5281/zenodo.7912742. [f]Except for HIRS/4 (10 km), noting also HIRS on Nimbus-6 is not covered here. [g]Note that AVHRR Global Area Coverage (GAC) data used in the present work present a lower resolution.

Taking note of this inter-relation between reanalysis and the radiance data records, the following remediation steps are taken. (1) For MVIRI we only show results before the date when MVIRI radiances started being assimilated in ERA5. (2) For SEVIRI we do not simply consider departures (differences between observed radiances and simulations), but consider how they vary by changing the simulation setup. (3) For HIRS we do not consider the departures alone but along with AVHRR, and we also exploit the departures at a time-scale for which we believe there is independence between the satellite data record and the reanalysis.

2.4 Quality controls

2.4.1 Observations

Observations with missing geolocation, brightness temperatures, or reflectances (in the case of AVHRR visible and near-infrared channels) are excluded from further analysis. In addition, specific quality controls are applied to the data records of each instrument, using the information available. For completeness, the details are reported in Supplement Text S1.

2.4.2 Simulations

The performance of radiative transfer simulations can be degraded in several situations. These are indicated in this sub-section, along with measures to mitigate these degradations.

Performance degradation of the simulations may occur in situations of Non-Local Thermal Equilibrium (NLTE) if this effect is not specifically accounted for. Such degradations, which arise during daytime in modelling short-wave infrared channels, are excluded from the analysis; for the corresponding HIRS, AVHRR, and SEVIRI channels (with wavelengths in the region 3—4 μm), we follow a conservative approach, retaining only cases when the sun is below the horizon by at least 10 degrees. Similarly, the performance of RTTOV may be degraded for situations of specular reflections. Consequently, in the AVHRR visible and near-infrared channels simulations, cases in which the sun is low on the horizon are discarded from the analysis (we retain only cases when the sun is above the horizon by more than 10 degrees).

The performance of radiative transfer simulations is also degraded when the presence of clouds (infrared and visible) or precipitating clouds (microwave) is not accounted for. As all simulations are carried out assuming clear sky conditions, we need to apply a filtering to exclude cloudy situations (infrared and visible) or precipitating clouds (microwave). For simplicity, we use the generic term ‘cloud mask’ in all cases, even if there are distinct differences in the implementations. These implementations are described now.

In the absence of a single cloud mask for all instruments at all dates and times, the cloud filtering approach depends on the instrument. The presence of clouds and/or precipitation is filtered in three cases in this study.

In the first case, a cloud mask is available for the instrument’s data record. This applies to AVHRR (Karlsson et al., 2023), MVIRI (Stöckli et al., 2019), SEVIRI (EUMETSAT, 2015), and SSM/T-2 (EUMETSAT, 2021). In the case of SSM/T-2, the cloud mask uses information retrieved from SSM/I observations by the EUMETSAT Climate Monitoring SAF (CM-SAF) (Andersson et al., 2017), albeit only available over oceans.

In the second case, the availability of a window channel (i.e., a channel affected only weakly by atmospheric absorption) enables use of the departure window method check, similar to the approach typically employed by data assimilation (Krzeminski et al., 2009). In this method, a departure outside a predefined range is indicative of the presence of cloud. This method works better over ocean than over land, affected by greater uncertainties in sea-surface temperature and emissivity, and is applied over ocean region for filtering out clouds from SI-1 observations. The range of allowed window channel departures is set to [-2 K, 3 K], as the SI-1 instrument operated before the well-observed satellite era, and when the quality of reanalyses is known to be poorer (e.g., Bell et al., 2021). The SI-1 channels considered for this check are between 882 cm^{-1} and 916 cm^{-1}.

In the third case, when neither of the two approaches above is applicable, but the effects of clouds or rain need to be filtered out, we devise proxy criteria to identify pixels affected by these situations. These criteria are presented afterwards, for MRIR and SMMR.

Additional details on the application of the cloud masks are presented in the relevant sections hereafter as relevant.

2.5 Departure analysis

The general philosophy for analyzing the results is to follow the split-apply-combine method (Wickham, 2011), preceded by the quality control steps mentioned previously. Hereafter, we consider two statistics of the departures (observations minus simulations): the mean (noted μ) and the standard deviation (noted σ). Both quantities are in K for brightness temperatures, or in % for reflectances (for visible or near-infrared channels).

3 Class-I applications: Validating an assumption

When developing a dataset or an application, it is common to be faced with the issue of validating an assumption used in the methodology. The assumption could, for example, relate to the data themselves, or how to use them. However, a common difficulty is the impracticality of proving the assumption. One can then revert to demonstrating that the assumption is not violated, based on the evidence available. If the results obtained violate the assumptions, then the assumption is proven wrong. If they do not, then the assumption cannot be rejected, and is hence considered to remain valid.

3.1 Advanced image quality control, example with Meteosat geostationary imagers

The Meteosat First Generation (MFG) satellites started the first series of continuous imaging over Africa and Europe (e.g., De Jong, 1978). The resulting images brought about new understanding of the weather patterns, but also uncovered a number of challenges for image processing that were unforeseen when the instruments were designed. The analysis of the resulting data record is impacted by so-called “image anomalies” (IA), which, for example, lead to under- or over-estimation of the radiance at the scene. This term is to be understood distinctly from its climate counterpart, where an anomaly is defined as the difference of a quantity with respect to some climatology. In the case of instrument operations, IA refers to an unexpected behavior that would cause improper interpretation of the image. As there is no reason to expect that such effects should cancel out, it is important to identify data affected by instrument issues, to avoid introducing spurious signals into long-term series. Several IA issues were not foreseen when the MVIRI instrument was initially designed. Methodologies to detect geostationary IA were developed over the years (e.g., Liefhebber et al., 2020) and cover a wide range of situations, from simple cases of complete image data corruption to more complex situations of regional over-illumination.

If these image anomalies are correctly detected, masking out such problematic areas or images should lead to an improved agreement between images and other sources of information, such as radiative transfer from simulations. We verify this here in Figure 1 for a randomly picked date (1996-10-16) among dates when images anomalies were detected, from the MFG data record of Meteosat-5. Figure 1(a) shows a map of all the departures before any cloud or image anomaly filtering. Figure 1(b) shows the results after applying a cloud mask (Stöckli et al., 2019). It can be seen that cloud masking improves the agreement between observations and

simulations significantly, by reducing the standard deviation of differences over the full image from 5.4 K to 1.9 K and by bringing the mean of differences closer to zero, from -0.7 K to 0.3 K. Figure 1(c) shows the results after filtering out scenes affected by an IA. In this case, the IA filtered out is direct stray light and over-illumination as defined by Liefhebber et al. (2020). The results indicate that this reduces the data count over the entire image by around 10%, but the agreement between observations and simulations is improved, with a standard deviation of differences reduced from 1.9 K to 1.4 K, and a mean reduced to near-zero.

In summary, the radiative transfer simulations help us validate the assumption that an advanced image quality control should improve exploitation of the MVIRI data record.

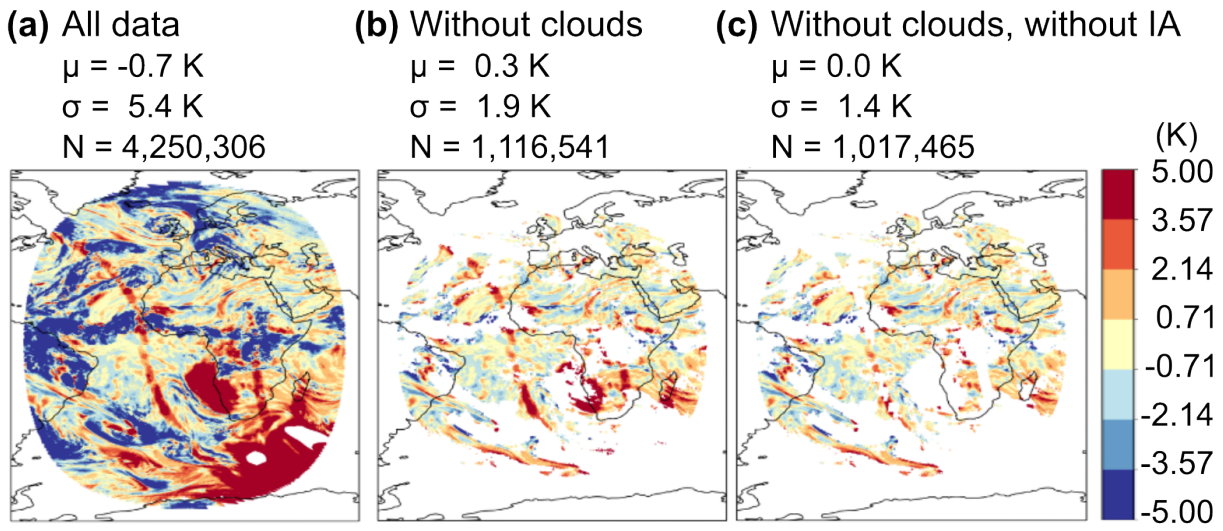

Figure 1. Maps of differences (in K) between observations and radiative transfer simulations using ERA5 for Meteosat-5 MVIRI water vapor channel, 1996-10-16 00 UTC: (a) all data, (b) results after excluding scenes believed to be cloudy, and (c) results after excluding in addition the scenes affected by image anomaly (IA). Overall statistics are reported at the top.

3.2 Cloud mask, example with HIRS and AVHRR

An important objective of the assessment of the quality of satellite data records is to determine the quality of representation of climate time-scales. Such decadal products are of interest to users to study possibly small-scale variations over a long timeframe. There is a wide body of literature on data assessment (e.g., National Research Council (U.S.), 2004). However, from infra-red sounders and imagers, most retrievals schemes are restricted to clear-scenes only. For this reason, cloud mask validation is important.

Such activities are already performed routinely by cloud mask data producers. We show an example of how radiative transfer simulations can further assist in this fashion. To this end, we consider the infra-red and visible data records of two polar-orbiting instruments, the AVHRR and HIRS instruments, operated both on NOAA and EUMETSAT polar-orbiting satellites, and compare with clear-sky radiative transfer simulations.

The effects of clouds and aerosols are not included in the radiative transfer simulations considered here. Consequently, a large disagreement is expected around and after the time of the

volcanic eruptions that generated considerable amounts of aerosols in the atmosphere. However, the effects of volcanic eruptions alone may not necessarily stand out because of other effects, such as spatial variability and clouds (ignored in the simulations). For this reason, we focus the evaluation on small geographical regions, to avoid potential issues of large-scale inhomogeneities within the region. The regions are as defined in the IPCC 6th Assessment Report (Iturbide et al., 2020).

Figure 2 shows, for the Equatorial Pacific Ocean region, the results of differences for the mode of differences (maximum of the departure distribution within a month) between observations and clear-sky radiative transfer simulations. The results are shown without any prior filtering for clouds. To obtain these timeseries, we first construct monthly histograms of departures, for each satellite and each channel, with a resolution of 0.1 K for brightness temperatures (HIRS and AVHRR infra-red channels) and of 0.1 % for reflectance (AVHRR near-infrared channel). For each histogram, we then estimate the mode of the distribution. Finally, we look on either side of the peak for values that delimit the 88% of the peak maximum. This allows us to quantify a peak width, which would approximate the standard deviation of departures if the distributions were normal. This metric is shown with bars around the mode.

We present here window channels, (respectively) HIRS channel 8 (thermal infrared at 11.1 μm), HIRS channel 18 (shortwave infrared at 4.0 μm), and AVHRR channel 4 (thermal infrared at 11.0 μm). For these channels, the departures generally feature negative biases, as expected, owing to the presence of clouds. Figure 2(a,b,c) shows the agreement between these observations and ERA5 improves from 1991 onwards, thanks to Sea-Surface Temperature information of high quality obtained from the well-calibrated sensors (Advanced) Along Track Scanning Radiometer ((A)ATSR) on European Remote Sensing satellites ERS-1/2 (and Envisat), as well as subsequent sensors, such as the Sea and Land Surface Temperature Radiometer (SLSTR) on Sentinel-3. For the AVHRR near-infrared channel 2, the departures in Figure 2(d) are generally within 0.5 %, except for some satellite-dependent and volcanic eruptions episodes indicated by dashed vertical lines.

If the cloud mask is correct, we expect that its application would yield departures that are possibly closer to zero, depending on the reanalysis intrinsic biases, but also with a reduced standard deviation. Figure 3 shows this is indeed the case. Outside the volcanic eruption events, the standard deviations of departures (height of individual bars) are reduced from 0.6-0.8 K to 0.4-0.6 K. The modes of departures for the HIRS channel 8 in Figure 3(a) feature a declining trend in the 1980s, not seen with the channels shown in Figure 3(b,c). If the root cause of the trend was only with a trend in biases in the reanalysis (ERA5) used for the simulations, then a similar behavior would show on the other channels, too, but it is not the case. This would suggest that the recalibration of HIRS channel 8 may benefit from further refinements. Note the effects of volcanic eruptions stand out in all timeseries.

The relevance of a cloud mask needing not to be demonstrated further, we now investigate the departures around the time of the Mount Pinatubo eruption in more details. The use of AVHRR to monitor volcanic ash is well-established (e.g., Watkin, 2003). For all the window channels, increased negative departures are observed in Figures 2 and 3 panels (a)-(c) around the time of the El Chichon and Pinatubo eruptions, as expected, with aerosols scattering radiation and emitting radiation from above the surface (hence at a colder temperature). For Pinatubo, the cooling anomaly in terms of brightness temperatures is on the order of 1 K, for

short-wave and thermal channels alike, although the signatures differ somewhat between channels.

For the AVHRR near-infrared channel 2 (0.8 μm), reflectance departures are positive for 2 to 3 years after the event, between 2 and 5%, in Figure 2(d). This is also as expected, due to scattering caused by the aerosols (and not simulated here). Unfortunately, the combination of rejection of high solar zenith angles with the selection of only clear scenes leads to discard most of the data for AVHRR channel 2, resulting in the prevalent absence of results for clear-scene reflectances in Figure 3(d). We now turn to the spatial variability of this global event, by considering other IPCC regions.

Zooming in over a shorter time period (December 1990 – January 1994), Figure 4 shows that the plume of aerosols took several months to propagate away from its origin in South-East Asia. Considering the minimum observed in brightness temperature departures by the infrared window channels (rows (a) to (c)), the effect of the eruption was most pronounced over the Tropical Indian Ocean 3 months after the eruption (column (i)), and then over the Tropical Pacific 4 to 5 months after the eruption (column (ii)), and again later in the southern latitudes (6 to 8 months, columns (iii),(iv)), with a further delay in the Mediterranean (up to a year, column (v)). Considering the maximum observed in reflectance departures by the near-infrared channel, the effect of the eruption was most pronounced over the Tropical Indian Ocean, and was felt in southern latitudes 2 to 3 months later, or in the Mediterranean 5 to 6 months later. The effects of this eruption were analyzed in detail previously (Stenchikov et al., 1998). However, the results shown here quantify the relevance of this episode with respect to the HIRS and AVHRR data records.

To summarize, this example validates the hypothesis that the CLARA-A3 cloud mask can help to a) filter out cloudy scenes, and b) quantify the radiative effects of the Mount Pinatubo eruption in the HIRS and AVHRR data records, with a separation between regional and temporal variations, at the wavelengths covered by the channels selected here.

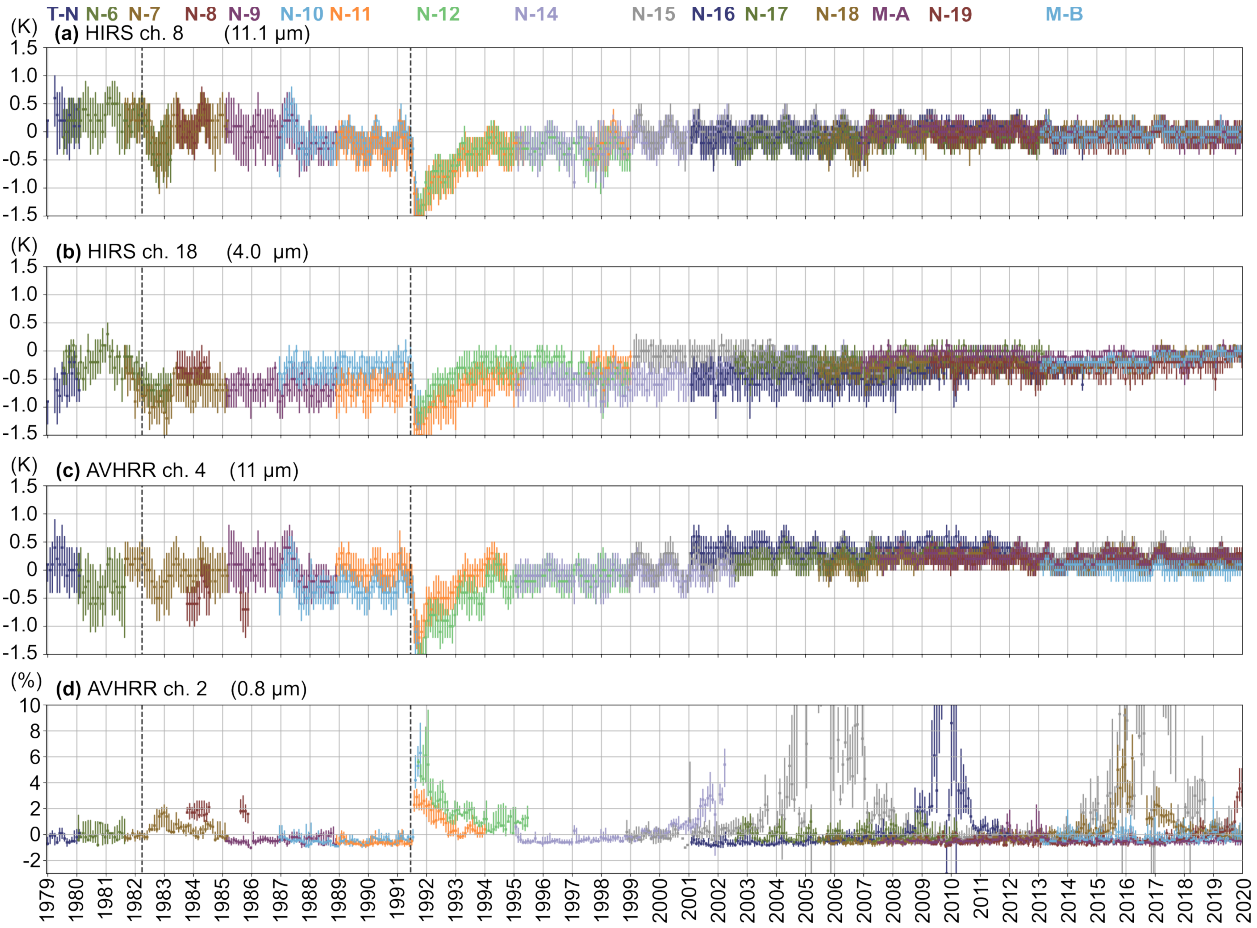

Figure 2. Monthly departures (modes as squares ± vertical bars to indicate spread estimates, see text) between HIRS, AVHRR and clear-sky radiative transfer simulations using ERA5, for the Equatorial Pacific Ocean region, between 1979 and 2020. Note two important volcanic eruptions: El Chichon (Mexico, 1982) and Mount Pinatubo (Philippines, 1991), with onsets indicated by vertical lines. Departures are shown for brightness temperatures (in K) for three infrared channels (a-c), and for reflectances (in %) for one visible channel (d). There is one color per satellite (from left to right, see top: T-N: TIROS-N, N-6 to N-19: NOAA-6 to -19, M-A and M-B: Metop-A and Metop-B).

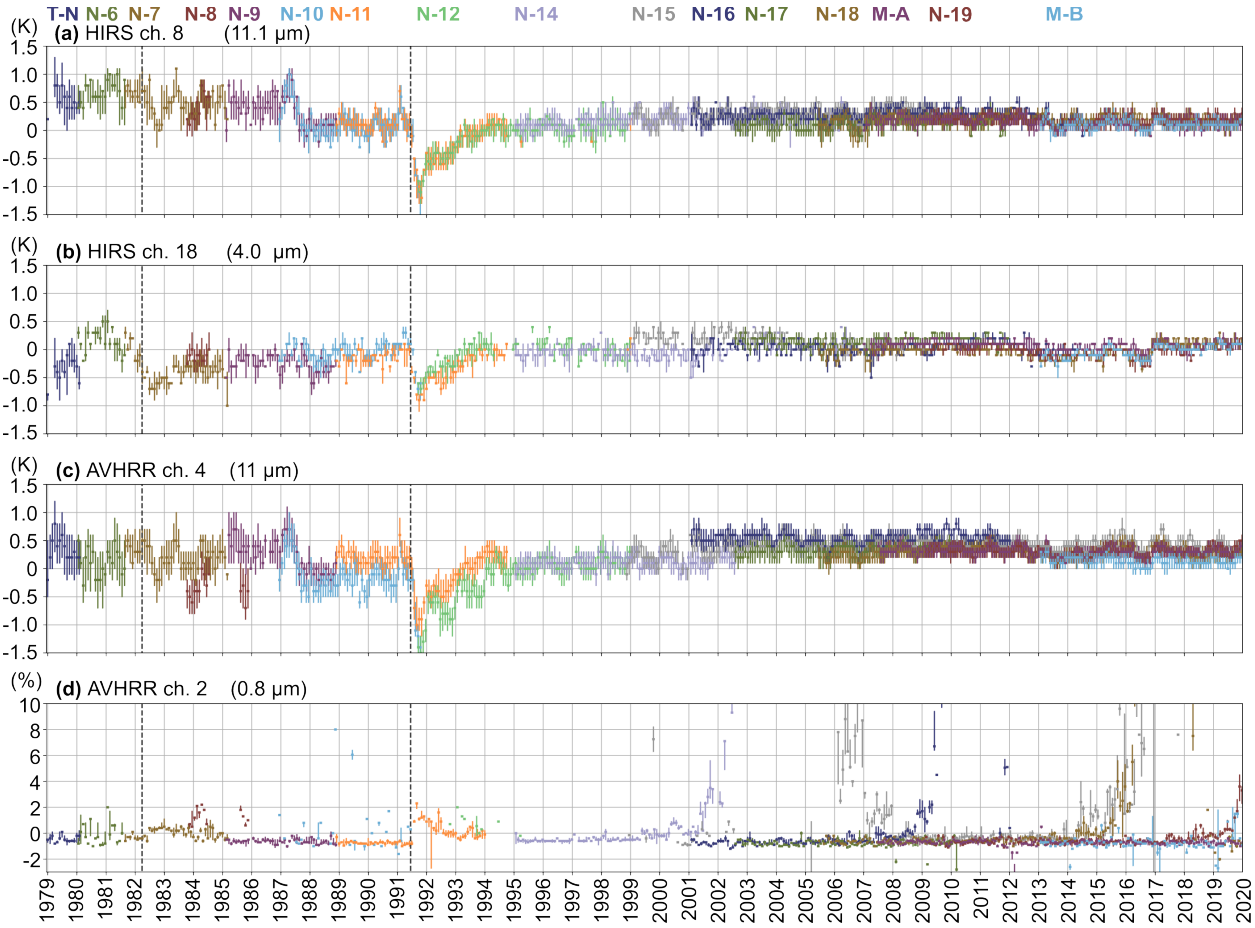

Figure 3. Similar to the previous figure, but restricting to scenes that are clear according to the cloud mask.

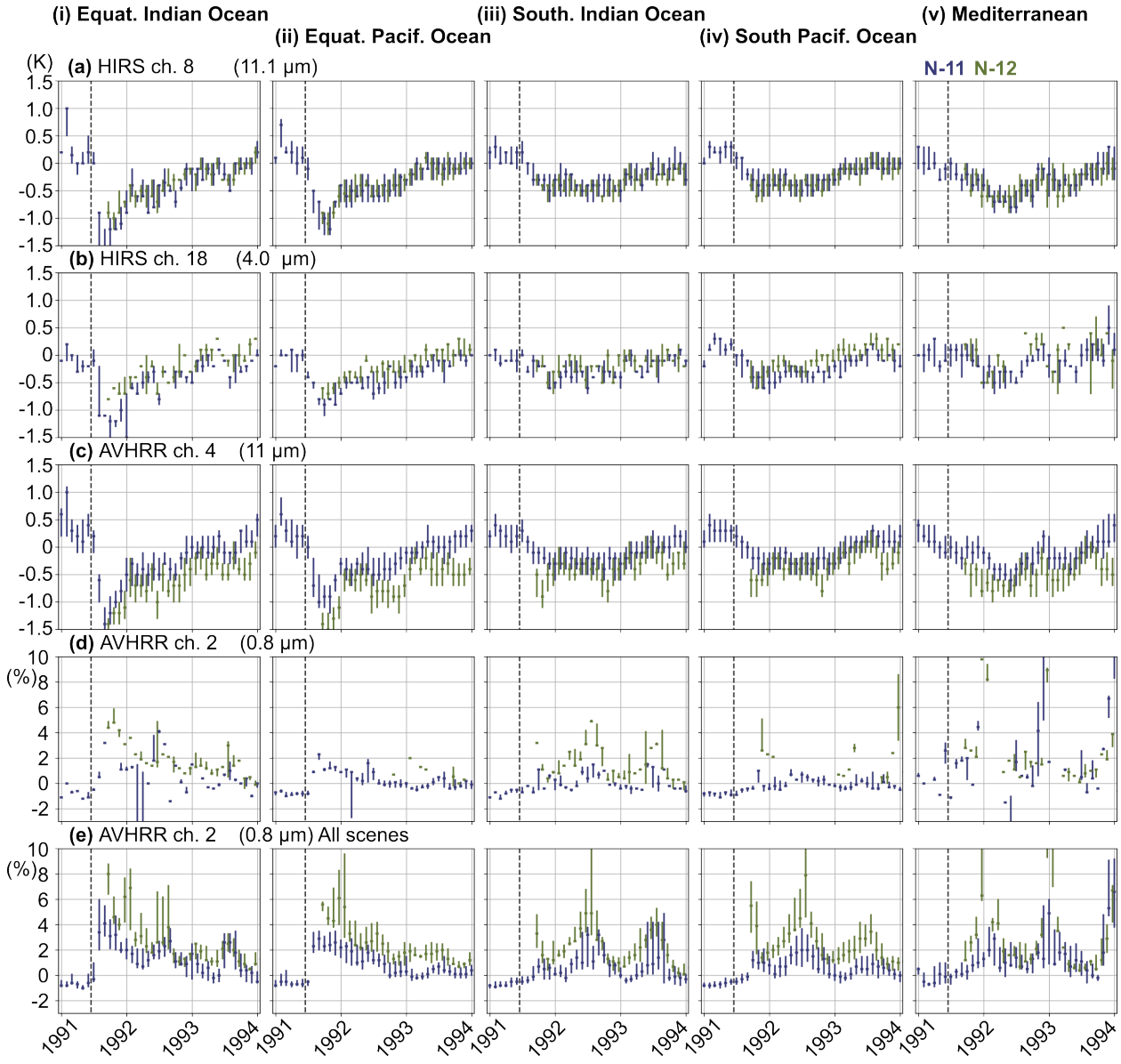

Figure 4. Similar to the previous figure, but showing several IPCC regions (see top, columns (i) to (v) from left to right) and zooming in on a time period starting six months before the Mount Pinatubo eruption (timing indicated by a vertical dotted line) and ending approximately 2.5 years after it. Note row (e) shows similar information as row (d) but for all scenes (i.e., without application of the cloud mask). There is one color per satellite (see top right, N-11 and N-12 for NOAA-11 and -12).

4 Class-II applications: Assessing coherence between reanalyses and observations

4.1 Synoptic timescales coherence, example with SI-1

The SI-1 instrument was a Michelson interferometer developed in the former German Democratic Republic, pursuing similar scientific objectives as the Infrared Interferometer Spectrometer (IRIS) instruments on-board Nimbus satellites covering the wavenumber range from 400 cm^{-1} to 1600 cm^{-1} (Hanel et al., 1970, 1972). The first IRIS instrument was launched a few years earlier than the SI-1 instrument . More particularly, the SI-1 instrument was designed to allow identification of atmospheric constituents, clouds, as well as temperature sounding (Kempe, 1980; Kempe et al., 1980) as well as planetary exploration, as a similar instrument was deployed in the atmosphere of Venus (Oertel et al., 1985).

Most of the 579-channel data record from this instrument has been rescued by EUMETSAT (Théodore et al., 2015), and the comprehensive data record is being prepared for public data release with support from the European Union Copernicus Climate Change Service (C3S) at the time of writing. Figure 5 shows the spectral range covered by the instrument, and the vertical sensitivity of the channels to atmospheric information. The SI-1 instruments operated discontinuously in time and the resulting data record is too sparse to support consistent data assimilation in a global reanalysis. However, high-resolution spectral features are potentially useful to better understand subtle changes in the climate (e.g., Brindley & Bantges, 2016).

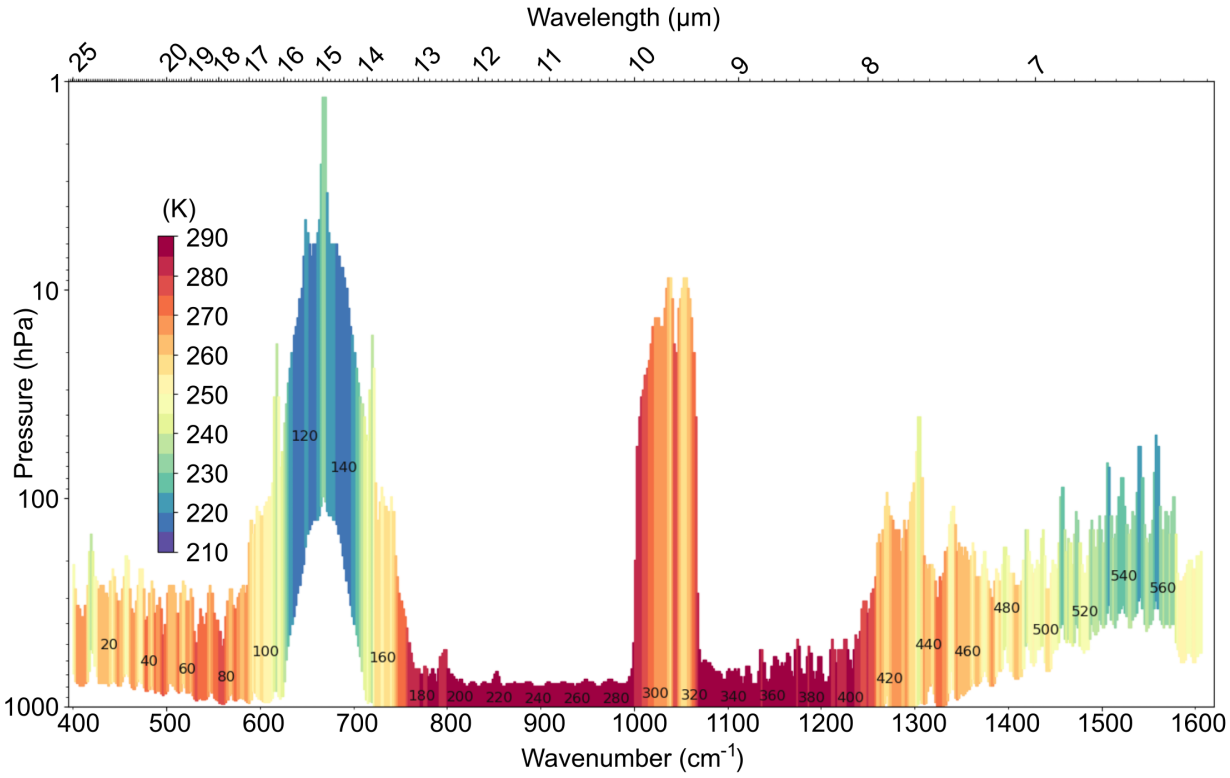

Figure 5. SI-1 wavelengths (top horizontal axis), wavenumbers (bottom horizontal axis), and RTTOV channel numbers (from left to right, in increments of 20). Each bar shows, horizontally, the nominal spectral resolution, and, vertically (bottom and top) the 5th to 95th percentiles (respectively) of the integrated weighting function, to help visualize where most of the atmospheric information comes from, for each channel, assuming clear-sky radiative transfer. Colors indicate the simulated brightness temperatures (in K, see scale). Calculations carried out from ERA5 data for a profile in the Spring over the Atlantic at the location (30°N, 30°W).

Another potential application of the SI-1 brightness temperatures is to use these to validate different reanalyses. We show an example here by considering a subset of the data record. Figure 6(a,b) shows the comparison of brightness temperature between observations and different reanalyses, for data at wavenumbers 400—1200 cm^{-1} collected by Meteor-29 over sea during the month of February 1979, for scenes to be believed free of clouds (123 spectra in total). The two panels separate between spectra that feature sharp departures (spikes) at wavenumbers 840—860 cm^{-1} and 765—810 cm^{-1}, across all reanalyses considered here. The reanalyses are ERA5, ERA-20C, JRA-55, and a preliminary version of the JRA-3Q reanalysis (a newer reanalysis as compared to JRA-55). For a fair comparison of the results, the ERA5 reanalysis profiles are considered every 6-hours, with a validity time window of ± 3 hours, like the other reanalyses (hourly ERA5 profiles at non-synoptic hours are ignored). The lower panels in Figure 6 show these departures. In a given column, the use of the same color across plots enables to appreciate that some degree of agreement exists sometimes between the reanalyses.

Considering all the spectra shown in Figure 6, Figure 7(a) shows mean differences between SI-1 brightness temperatures and the reanalyses. The standard deviations of departures are shown in Figure 7(b). The dotted lines in these figures show statistics of departures between

observations and simulations in radiance space, converted from difference radiance to equivalent difference brightness temperature at a nominal temperature of 280 K. Small differences with brightness temperature statistics are mostly visible where the brightness temperatures vary notably from this nominal temperature (see Figure 5), i.e., for the top-peaking channels in the middle of the 1041 cm^{-1} ozone absorption line or 667 cm^{-1} CO_2 absorption line, both sensitive to stratospheric temperatures. In this region, we find an agreement around 0.7—0.8 K in terms of equivalent difference brightness temperature (at 280 K) standard deviation.

Spikes are believed to be due to improper assumptions for trace gas concentrations in 1979 in our simulations. This is the case in particular near 845 cm^{-1}, an absorption line of trichlorofluoromethane, also known as CFC-11 (e.g., Harrison, 2018). Similarly, a bulge in standard deviations is visible between 765 and 810 cm^{-1}. Zenith absorption spectra, such as reported in the Atmospheric Infrared Spectrum Atlas (King & Dudhia, 2017), indicate strong absorption features near 775 cm^{-1} (COF_2), 780 cm^{-1} and 810 cm^{-1} ($ClONO_2$), 785 cm^{-1} ($CClF_3$, also known as CFC-13), 795 cm^{-1} (CCl_4), 810 cm^{-1} ($CHClF_2$, also known as HCFC-22), and 780—805 cm^{-1} (peroxyacetyl nitrate, $CH_3C(O)OONO_2$, also known as PAN). All these chemical constituents have seen large changes in concentrations over past decades owing to industrial emissions. Differences between present-day concentrations and those actually present in 1979 may be responsible for the departures reported here. Additional radiative transfer simulations, varying the absorber amounts, would help support investigations of such an hypothesis.

If the quality of JRA-3Q reanalysis improved as compared to the prior JRA-55 reanalysis, one would expect to see a better agreement with the simulations. The JRA-3Q improvements relative to JRA-55 in stratospheric ozone and stratospheric temperatures are clearly visible in Figure 7(a,b) around wavenumber 1041 cm^{-1} (sensitivity to stratospheric temperature and ozone) and wavenumber 667 cm^{-1} (sensitivity to stratospheric temperature). The standard deviations of departures in the region 600-700 cm^{-1} in Figure 7(b) also show that ERA-20C is an outlier, as compared to the other reanalyses, in terms of its fit to stratospheric-peaking channels located near the center of the line.

Having noticed in Figure 6 that spectral departures are sometimes similar across reanalyses, we apply similar concepts as those that underlie common uncertainty diagnostics (Desroziers et al., 2005). Assuming that all random uncertainties are independent from one another, we can estimate random uncertainties (see Supplement Text S2). Figure 7(c) shows the combined random uncertainties in the observations and radiative transfer (or representativeness), with a floor level in the range 0.8—1.0 K for most channels between 600 cm^{-1} and 1200 cm^{-1}. We interpret spectral sharp departures above that floor level as deficiencies in the radiative transfer assumptions (e.g., incorrect absorber concentration, which yields departures that are correlated across all reanalyses, even though departures differ between different profile locations and dates and times).

Going from high to low wavenumbers, we observe an increase of the combined random uncertainties in the observations and radiative transfer (or representativeness). One may postulate that this increase is related to instrument noise. However, our random uncertainty estimation method does not separate between random instrument noise and random uncertainties in the radiative transfer model. Consequently, it could also be that the radiative transfer model is deficient in this region of the spectrum. There is indeed far less experience with observations of this far-infrared region of the spectrum than at wavenumbers in the range 650—1600 cm^{-1}. This

situation should improve in future years with the Far-infrared Outgoing Radiation Understanding and Monitoring (FORUM) (Pachot et al., 2021). The FORUM instrument will indeed cover the spectral range between 100 and 1600 cm^{-1} (wavelengths between 6.2 and 100 μm) at 0.3 cm^{-1} of spectral sampling (5001 spectral elements).

Regarding the reanalyses, the estimates of random uncertainties are marked with crosses when the sum of squared uncertainties does not match the observed departure variance within a margin of 1% (this only occurs for some wavenumbers, in the region 620—750 cm^{-1}). Overall, we note that in most cases the findings agree with the considerations above, i.e. the expectation that the ERA-20C reanalysis contains much less pertinent information in terms of thermal vertical structure than the other reanalyses shown here, and that JRA-3Q made significant improvements regarding stratospheric representation quality as compared to JRA-55.

An important caveat of our method is the assumption of independence of random uncertainties, i.e., that cross-correlations between different uncertainty sources are zero. This may not be the case for a number of reasons, explained in the Supplement Text S2. In particular, the small spread between reanalyses may not reflect the true uncertainty but rather that these reanalyses share common uncertainties. For this reason, we believe that departures from this assumption are responsible for the very low level of random uncertainties (sometimes under 0.5 K) found for reanalyses. Conversely, some the uncertainties attributed to observations and radiative transfer (blue curve in Figure 7(d)) may actually come from uncertainties that are shared across the reanalyses, and hence may be over-estimated. Overall, we acknowledge that our method is not perfect but it still provides some initial insight into the uncertainties, which is a first for data collected by this early interferometer.

To summarize, this example illustrates how a high spectral resolution record, even when it is only short, can assist to measure progress in reanalyses.

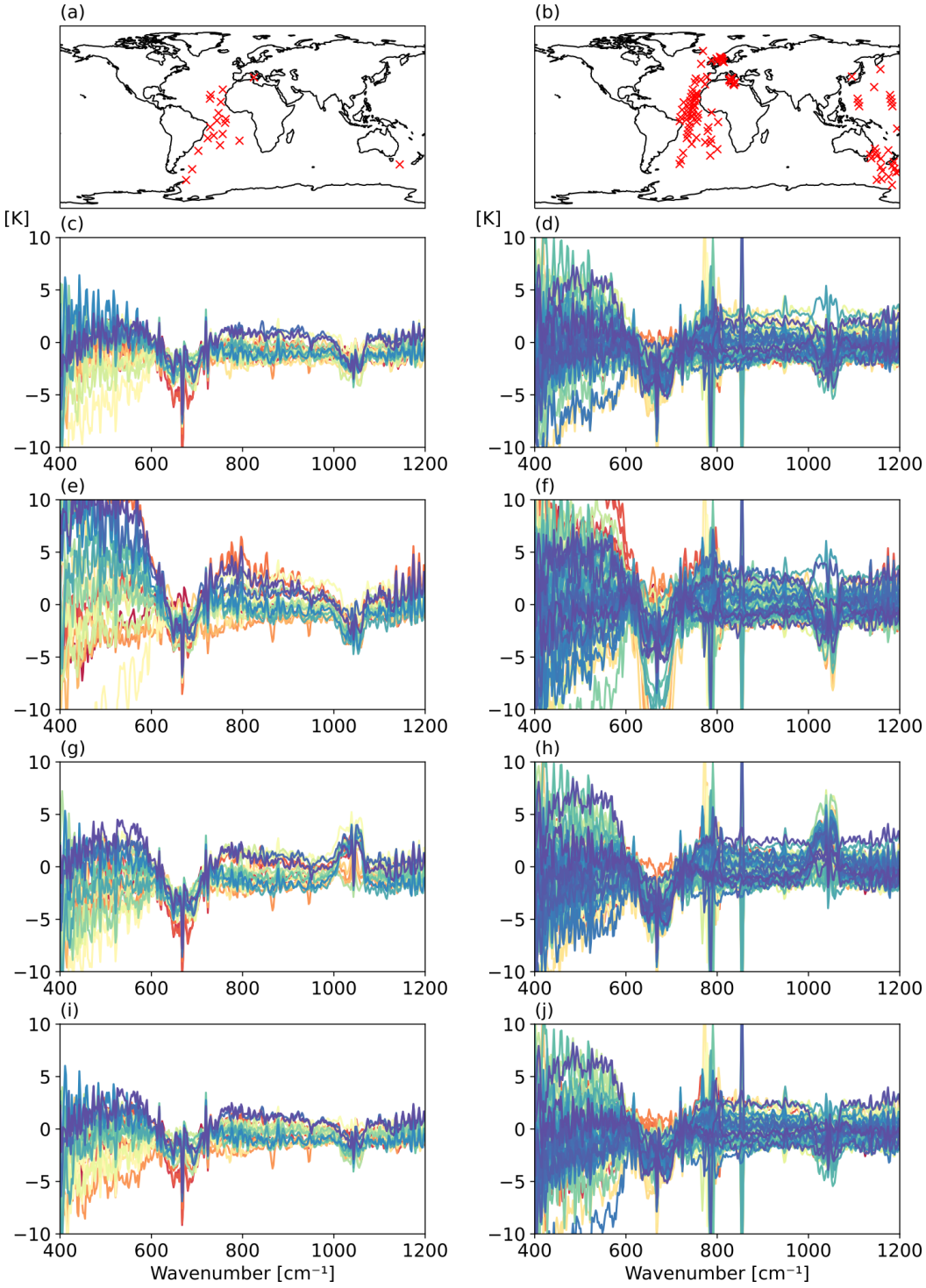

570

571 **Figure 6.** (a) Map of 19 Meteor-29 SI-1 observations in February 1979 without significant
572 spectral spikes in regions 840—860 cm^{-1} and 765—810 cm^{-1}, and (b) map of 104 other Meteor-
573 29 SI-1 observations presenting such spectral features. Bottom plots show corresponding
574 differences in brightness temperature between observations and simulations, using (c,d) ERA5;
575 (e,f) ERA-20C; (g,h) JRA-55; (i,j) a preliminary version of JRA-3Q.

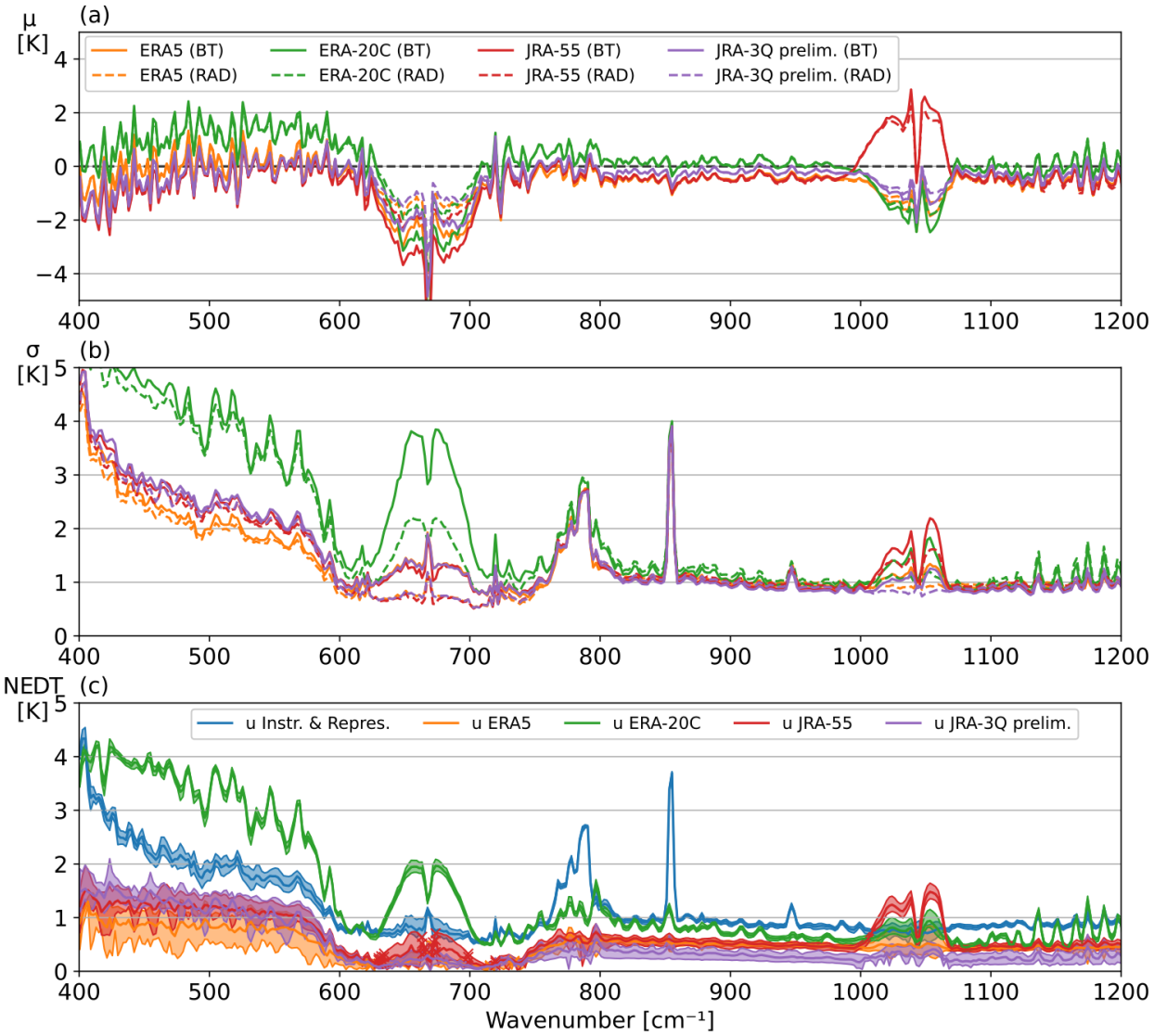

Figure 7. Departure (a) means (μ) and (b) standard deviations (σ) of Brightness Temperature (BT) differences between 123 Meteor-29 SI-1 spectra shown in the previous figure and corresponding radiative transfer simulations using ERA5, ERA-20C, JRA-55, and a preliminary version of JRA-3Q (see legend). Dotted lines show similar statistics but based on radiance (RAD) differences, converted from difference radiance to difference brightness temperature at a nominal temperature of 280 K. Bottom plot (c) shows estimates of random uncertainties (u), separating between each reanalysis random uncertainty, and combined observation and representativeness random uncertainty (see legend, and refer to text for details).

4.2 Understanding differences via bias correction linear predictors, example with MRIR

Bias correction methods aim at removing low-frequency variability in differences between observations and models, believed to be caused by systematic errors, for example, in the radiative transfer model or the instrument calibration (e.g., Dee & Uppala, 2009). In data assimilation, where radiance simulations are based on atmospheric profiles provided by a background, the methodology for such bias correction is now well-established. The bias is

591 modelled as a linear combination of a set of predictors. Based on linear regression models, i.e.,
592 one of many methods used in machine learning (e.g., Mitchell, 1997), bias corrections are thus
593 effective tools to understand patterns of differences between observations and simulations.

594 For the infrared channels of the MRIR instrument, we investigate here the performance of
595 extending the predictor set to include parameters believed to be at least in part related to
596 instrument error. This analysis is restricted to daytime and ocean data only. Observations of the
597 visible channel of MRIR are used to screen clouds, by excluding observations with an albedo
598 greater than 0.1.

599 We compare the bias correction performances of three different bias predictor sets. The
600 first predictor set is similar to that used in ERA-Interim and ERA5. This set includes four air
601 mass predictors, in the form of geopotential layer thicknesses (1000—300 hPa, 200—50 hPa,
602 10—1 hPa, and 50—5 hPa). One notes that corrections related to air mass are unlikely to be
603 instrument-related, and may more closely relate to errors in the simulations (i.e., reanalysis in the
604 present case). This predictor set also includes an offset, as well as the satellite viewing angle and
605 its squared and cubed values. These four additional predictors are all expected to capture
606 instrument and simulation errors, although noting the cubed value may capture foremost
607 simulation errors. Note, the viewing angle is a parameter which may partly absorb calibration
608 errors (e.g., Buehler et al., 2005).

609 The second predictor set is the so-called instrument predictor set. It excludes some of the
610 predictors mentioned above that are believed to capture mostly simulation errors (layer
611 thicknesses and satellite viewing angle cubed). However, it adds scene brightness temperature
612 and instrument internal temperature. These two additional predictors are introduced to account
613 for instrument errors due to uncertainties in gain and non-linearity effects, and instrument-
614 temperature-related errors (respectively). Note, the scene brightness temperature is also expected
615 to absorb some of the simulation errors.

616 Finally, the third predictor set considered combines all predictors of the first and second
617 predictor sets.

618 Figure 8 shows the effects of applying the three bias predictor sets. The metric that is
619 chosen for this assessment is the standard deviation of the Nimbus-3 MRIR departures (σ). The
620 mean departures, not shown, are reduced to near-zero in all cases, by design of the bias
621 correction. The figure shows results without bias correction (blue), after applying the ECMWF
622 predictor set (orange), the instrument predictor set (green), and the combined predictor set (red).
623 As might be expected, all bias-corrected results fare better than the uncorrected case. In addition,
624 the ECMWF and instrument predictor sets have similar impacts. The combined predictor set
625 performs best of all. Especially for 10.5 μm and 15 μm channels there are significant
626 improvements to the standard deviations (note the factor two improvement for the 15μm
627 channel). This indicates that both simulation and observation errors are significant. This also
628 suggests that further studies of instrument-related departures should provide useful insights into
629 the state of the instrument calibration.

630 In the case of the MRIR it is difficult to go beyond the bias correction models shown in
631 Figure 8 as we lack the low level telemetry data (Level 0 data) that are needed to correct for
632 instrument calibration errors at source.

In summary, this example shows that improvements may be made for MRIR to the bias correction models generally used in data assimilation, by considering likely instrument sources of uncertainties.

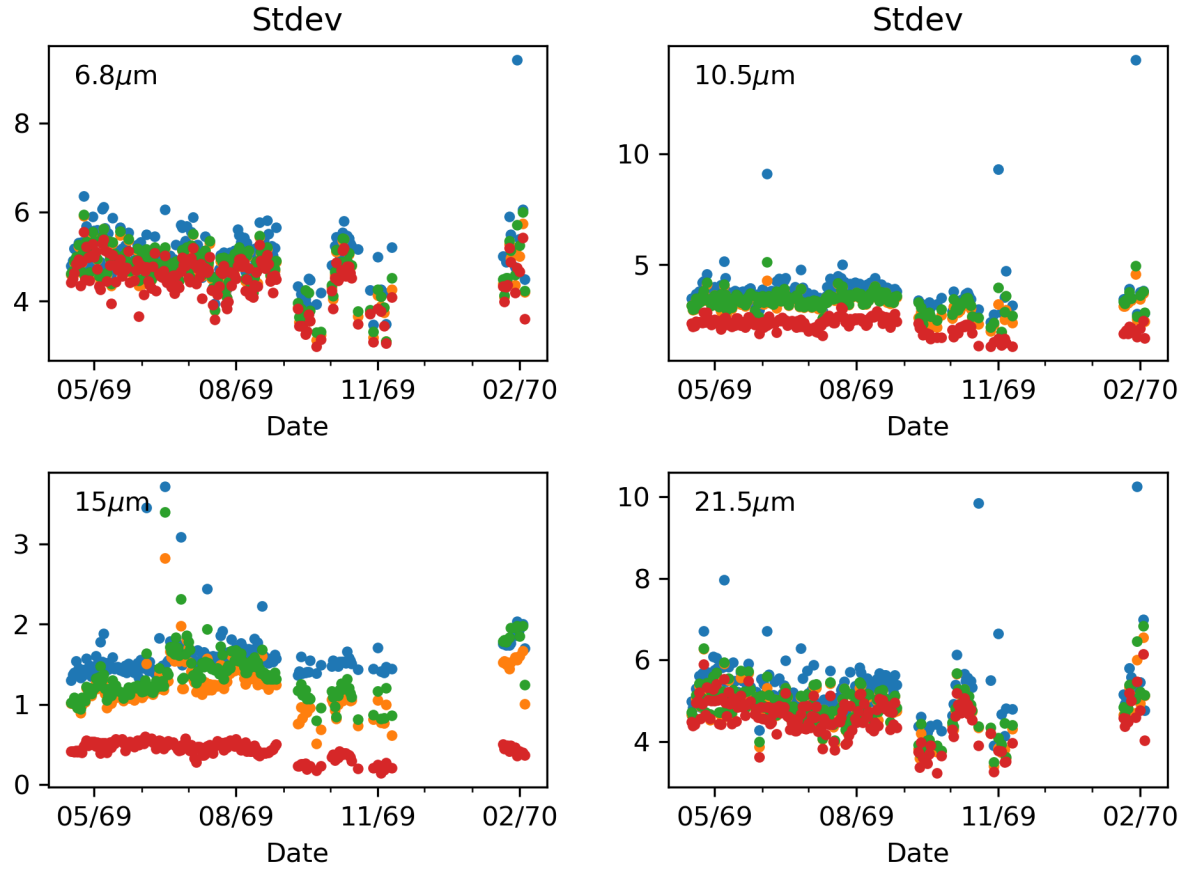

Figure 8. Time-series of daily Nimbus-3 (1969-1970) MRIR departure standard deviations (σ, in K), for four different channels, without bias correction (blue dots), and with different bias correction schemes applied: ECMWF predictor set (orange dots), instrument predictor set (green dots) and combined predictor set (red dots). See text for details.

5 Class-III applications: Informing users

5.1 Unexplained observation variability, example with SMMR

The microwave radiometer SMMR was a pioneering instrument for several fields in the Earth sciences. Two flight models were launched in 1978. The satellite carrying the first SMMR unit, Seasat, malfunctioned a few months after launch. The second SMMR unit, on Nimbus-7, operated for nearly 9 years, until August 1987. It offers an overlap, albeit limited, with the SSM/I (from July 1987). This particular time period is often looked at to enable inter-calibration of the two instruments' data records (e.g., Dai et al., 2015).

The SMMR instrument collected measurements at five microwave frequencies and two polarizations (vertical and horizontal). The complexities of this instrument and the resulting data

record stem from the use of six radiometers to monitor ten channels. This prevented continuous monitoring of all ten channels for all footprints. Instead, the instrument used four radiometers to monitor the lower frequencies (6.6 GHz, 10.7 GHz, 18 GHz, and 21 GHz), by alternating polarization at each half-scan, while two other radiometers continuously monitored the 37 GHz frequency, at vertical and horizontal polarizations. However, most physical retrieval schemes were devised assuming data available from all channels. For this reason, the data processing includes a re-sampling of the data to cover all footprints.

NASA carried out the first and only full SMMR reprocessing within the Pathfinder project that was completed in the late 1990s (Njoku, 2003). This reprocessing included corrections for antenna pattern and polarization mixing. The reprocessing also revisited important components of the processing and applied lessons learnt from the mission. This effort also unveiled new elements to address, such as a sharp change in Nimbus-7 spacecraft attitude in 1984, unaccounted for in this first reprocessing, as this issue was detected afterwards.

The CM-SAF (Fennig et al., 2017) further attempted to reprocess the SMMR data. However, they could not start from the original low-level sensor data, as these data could not be located at the time. This means that several of the benefits expected from a full reprocessing could not be realized.

In this section, the reprocessed SMMR data from the CM-SAF are compared against radiative transfer simulations from two reanalyses, ERA-Interim and ERA5. Figure 9 shows that all frequencies present mean departures that are similar for ERA-Interim and ERA5, on the monthly timescales shown here, for the horizontal polarization. The data counts differ from ERA-Interim and ERA5 as approximately 4 times more data are being assessed in the case of ERA5 (hourly) than in the case of ERA-Interim (six-hourly).

Over oceans, SMMR data with rainy situations are excluded by checking distributions of departures (heuristic approach). Observations are considered rainy if the difference between horizontally polarized channels 37 GHz minus 18 GHz is outside the range [30 K, 50 K], if the difference between horizontally polarized channels 6.6 GHz minus 10.7 GHz is outside the range [-15 K, -5 K], if the polarization difference (vertical minus horizontal) at 37 GHz is less than 35 K, or if the brightness temperature at 18 GHz (6.6 GHz), horizontal polarization, exceeds 160 K (95 K, respectively). Data over land are not further analyzed here.

Figure 9(d) indicates spurious oscillations in the mean departures with respect to both reanalyses, before the 21 GHz radiometer (channel 9) failed in 1985. The magnitude of these oscillations grows over time, as well as the standard deviations of departures. Until such a behavior can be explained, these features can be interpreted as symptoms of a degradation over time of the horizontally-polarized 21 GHz channel.

During a Special Operations Period (SOP) that lasted from 3 April to 6 June 1986, the SMMR instrument was operated in a different mode. Instead of functioning every other day, the instrument was switched on and off more frequently, up to several times per day. The statistics indicate that it took some time after the SOP for the instrument to recover to its pre-SOP status. The exact cause for this behavior is unknown, but is suspected to be related to the SOP. The observed degradation is reported by Njoku (2003) to have lasted “during and for some time after the Special Operations Period”. This element is apparent for all channels as shown in Figure 9. The difference in statistics before and after the SOP is indeed evident for most channels shown. This points to a change in the calibration performance of the instrument after the 1986 SOP. In

other terms, the data collected in 1987 may not be taken as representative of the instrument performance beforehand. Yet, the data from 1987 remain important as they are compared with SSM/I in order to inter-calibrate both records, as indicated above.

To summarize, we find issues of channel performance degradation, large oscillating biases, and changes in calibration performance after the 1986 SOP. This information is potentially important information for users interested in climate applications. These issues are however difficult to address at the level of retrieval into geophysical quantities. This would rather need addressing with a new recalibration and reprocessing activity.

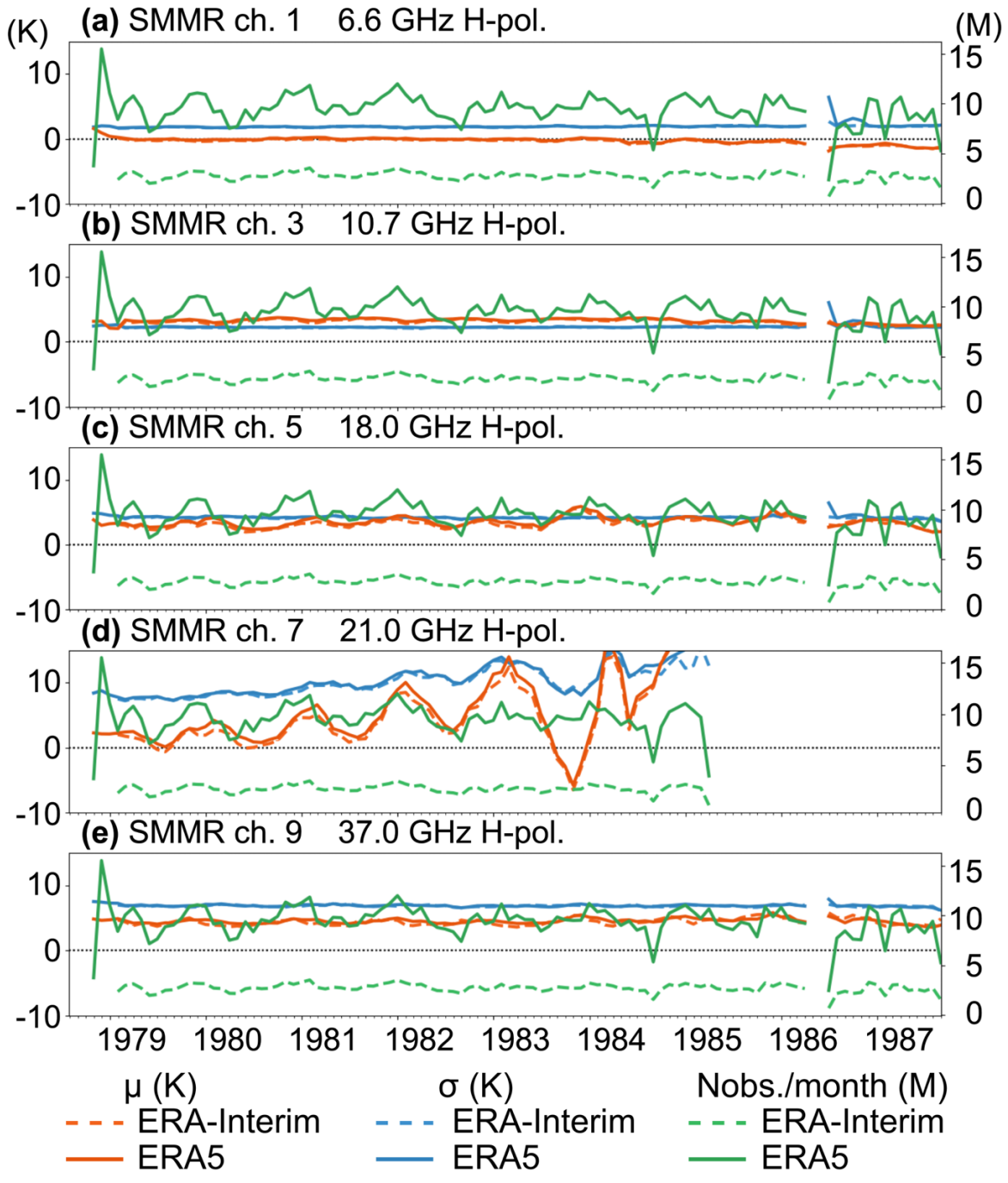

703

704 **Figure 9.** Time-series of monthly mean departures (μ, orange) and standard deviations (σ, blue)
705 between SMMR brightness temperatures and simulations using 6-hourly ERA-Interim and
706 hourly ERA5 fields (see legend), for horizontally-polarized channels at frequencies (a) 6.6 GHz,
707 (b) 10.7 GHz, (c) 18.0 GHz, (d) 21.0 GHz, and (e) 37.0 GHz, in K (left-hand-side vertical axis).
708 The data counts per month (green) are reported (in millions, M) on the right-hand-side vertical
709 axis.

5.2 Explained observation variability, example with MSG

The SEVIRI instruments on-board MSG satellites extend the data records started by MVIRI instruments on-board MFG satellites for the 3 heritage channels, i.e., the water vapor, infrared, and visible channels. Furthermore, SEVIRI includes 6 additional channels in the infrared region as compared to MVIRI. When the MFG and MSG satellites are positioned near 0-degree longitude, the field of view of the instruments covers Africa and Europe. Thus, the observed radiances of these satellites allow patterns of variability to be inferred over areas with important societal applications (e.g., Barbosa et al., 2019; Harrison et al., 2019).

Satellites in geostationary orbit are subject to small displacements around their nominal positions around the Equator. These satellites are affected by gravity pulls from the Earth and the Moon. This so called three-body system, or Lissajous track, results in figure-of-eight displacements (e.g., Hubert & Swale, 1984). In addition, geostationary satellites may see displacements during their lifetime when the nominal longitude changes. This section shows the importance for climate applications of these displacements (even if seemingly small), through an analysis of subsequent satellite data records that appear as originating from a single longitude position at the Equator.

The 15-minute MSG All-Sky Radiances (ASR) products are simulated here only for the two observation times closest to the hour (i.e., two images per hour are simulated, and two images are not). The quality controls applied selects only pixels that are believed to be free of clouds (so-called Clear-Sky Radiances, CSR), and for which the radiances are computed from an average of at least 10 pixels. These radiances are indeed horizontal averages of higher-resolution measurements.

The mean differences per month, as well as the standard deviations, between the MSG SEVIRI observations and the simulations based on ERA5, are shown for the whole observation area and for the two water vapor channels in Figure 10. In a first set of simulations, the nominal satellite position, at 0-degree longitude, is assumed. The resulting departures vary over time. Without any further indication to the contrary, a large part of these variations may be attributed to variations in the quality of the ERA5 reanalysis. In a second set of simulations, the radiative transfer simulations use as input the actual satellite position, as reported in the data, and thus can account for the effect of changing the viewing angle. This accounting has little impact on window channels (transparent to the atmosphere), but has some impact for channels measuring at the water vapor wavelengths. At these wavelengths the transmission is affected by the atmospheric optical depth. The comparison between Figure 10(c) and Figure 10(d) indicates that the actual satellite position gives a slightly better agreement with the data record. However, the magnitude of the changes may appear negligible at first sight.

For this reason, it is important to investigate in more detail how these changes manifest themselves. To this end, we compute mean differences per month between the two sets of simulations, at a resolution of 1^{o}x1^{o} latitude, longitude. This enables a Principal Component Analysis (PCA) to be carried out, using the differences between the two simulations. Prior to this analysis, these differences are normalized to zero-mean and unit standard deviation for each given satellite and each given channel (e.g., Aires et al., 2002). Figure 11(a) indicates that the first eigenvectors (EOFs) explain most of the variability in the differences. The maps of these differences in Figure 11(b,c,d) for the first three EOFs show the patterns of the differences. The temporal variations are also shown in Figure 11(e), showing distinct cycles.

Because of the prior normalization of differences, the patterns evident in Figure 11 appear more important than they manifested in observation departure space analysis (in K) of Figure 10. These patterns present distinct spatial and temporal aspects that may easily be misinterpreted in terms of climate evolution terms, should they appear from an analysis of the observed geostationary radiance data after removal of other effects.

In summary, this example stresses the importance of correctly accounting for the satellite viewing angles when considering geostationary radiance data from water vapor channels, for climate applications. If this is not done, then erroneous signals will propagate into downstream applications, and get aliased into the findings, possibly affecting conclusions that may be drawn about regional patterns of changes.

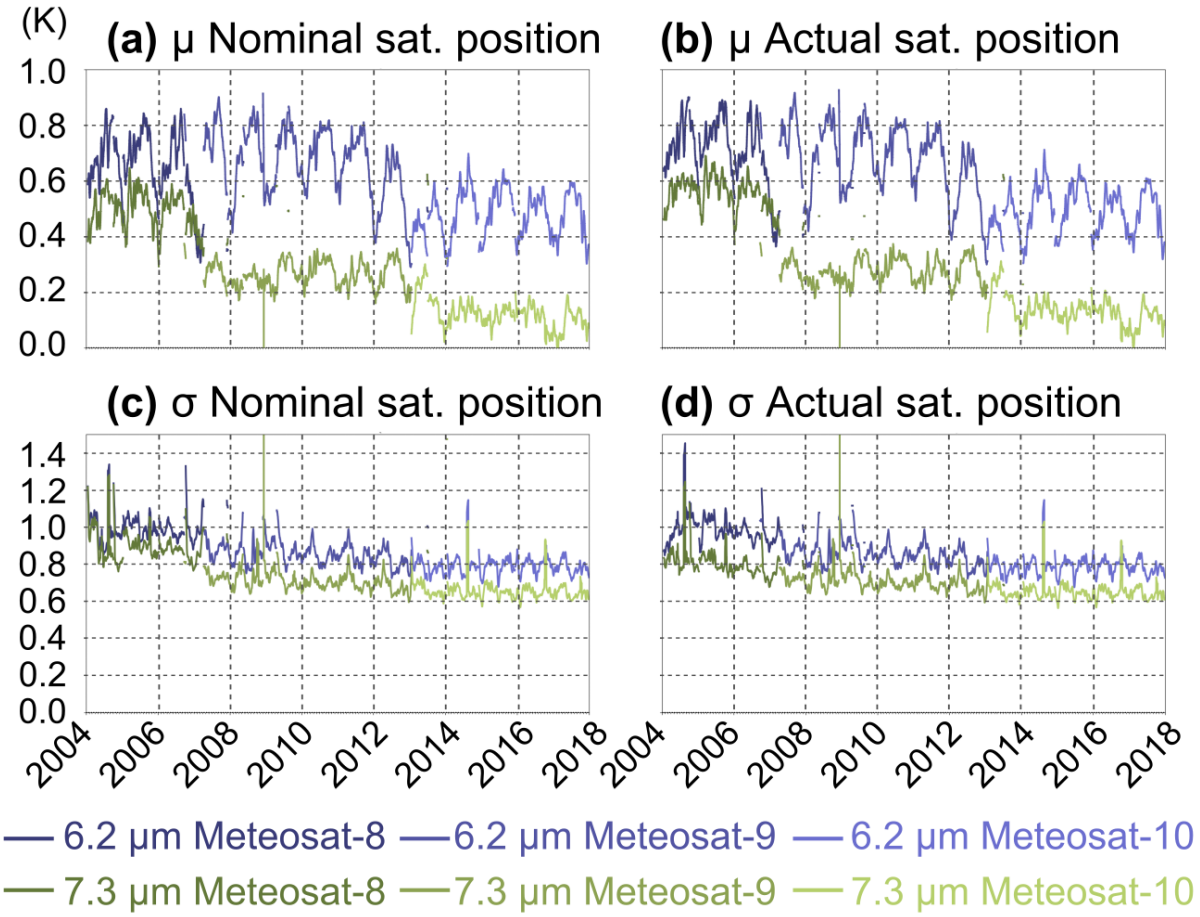

Figure 10. Time-series of (a,b) mean (μ) and (c,d) standard deviation (σ) of departures for SEVIRI water vapor channels, using two different methods for the simulations: (a,c) assuming nominal satellite position at 0 degrees longitude; (b,d) assuming the actual satellite position, as reported in the data.

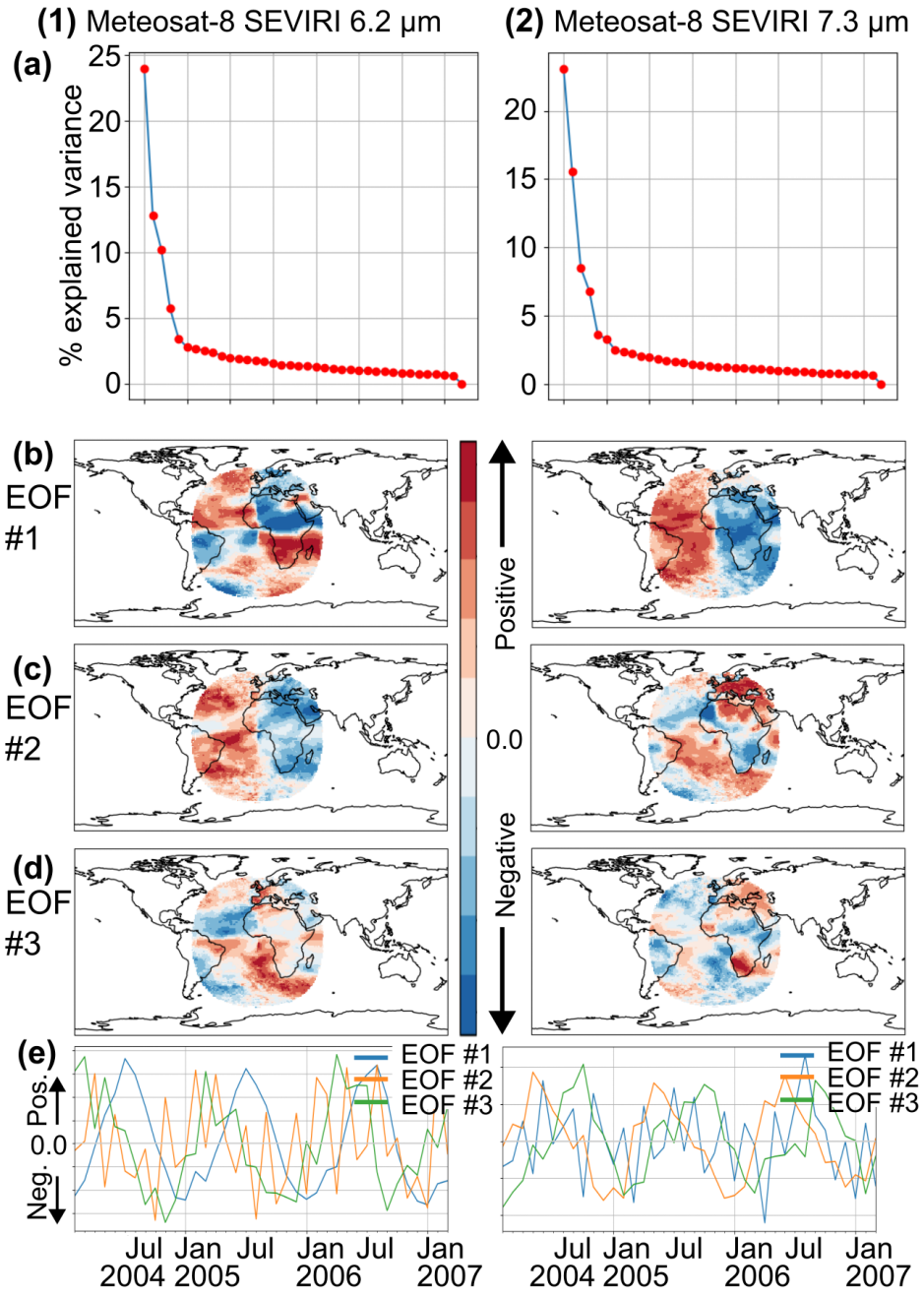

Figure 11. Results of PCA analysis of normalized differences between radiative transfer simulations (assuming actual satellite position minus assuming nominal satellite position), for two water vapor channels indicated in columns (1) and (2), as follows: row (a) shows the percentage of explained variance by PCA EOF, rows (b) to (d) show the spatial projections of the first 3 EOFs, and row (e) shows these EOFs' time-varying amplitudes. Note that because of normalization the patterns of amplitudes are to be interpreted qualitatively in spatial terms or temporally (e.g., frequency and phase). To further avoid mis-interpretation into actual departures (in K) the normalized amplitudes of EOFs are shown without numerical axes.

778 5.3 Relevance of uncertainty and observation horizontal local variability in a data record,
779 example with SSM/T-2

780 The SSM/T-2 microwave sounder data record was reprocessed by Hans et al. (2017),
781 including estimates of uncertainty for the antenna temperatures. A later release of these
782 reprocessed data included a cloud and rain mask (EUMETSAT, 2021), as these phenomena are
783 known to hamper the ability to use the 183 GHz data for water vapor retrieval. The analysis
784 presented in this section focuses on these channels.

785 The Quality Evaluation Report associated with the SSM/T-2 data record (EUMETSAT,
786 2021) shows that data present a few episodes of larger noise, most notably for the F-14 satellite
787 after 2001. This total uncertainty information is shown in Figure 12. Using this information,
788 episodes of increased noise may be removed by excluding all observations where the average
789 total uncertainty exceeds twice the pre-launch noise equivalent delta temperature (NEDT)
790 specifications of the given channel. The time periods that are removed by this procedure are
791 shown in the same figure.

792 Hereafter we show that the uncertainty information helps to pinpoint other effects in the
793 data. To this end, we consider the observation horizontal local variability (Δ), computed as the
794 standard deviation of the observations over a 3x3 horizontal array of neighboring pixels. We
795 further restrict our analysis to latitudes between 40^{o}S and 40^{o}N. This is to ensure the data large-
796 scale variability is driven by water vapor content and not by surface-induced emissivity, which
797 may be more poorly simulated in some situations, e.g. over sea-ice. We then bin all the results
798 according to the observation horizontal local variability (Δ), in bins of 0.1 K. For each bin, we
799 compute the data distribution (number of results found), as well as the mean and standard
800 deviation of departures. The results are shown in Figure 13. The peaks in the data distributions
801 indicate that the instruments have comparable noise characteristics. These peaks are situated in
802 the region of 0.6 to 0.8 K, which is in line with the instrument NEDT specifications. The gradual
803 increase in standard deviations as a function of observation horizontal local variability is also to
804 be expected.

805 The mean departures in Figure 13(a)-(c) are not all aligned with each other, but present
806 some (steady) offsets, depending on the satellites. This is most probably caused by the fact that
807 Antenna Pattern Corrections (APCs) were unknown and thus were not be applied during the
808 reprocessing. An alternative explanation for these offsets could be varying amounts of humidity
809 biases (over time) in the ERA5 reanalysis. Such small inter-satellite differences are not believed
810 to be a problem for applications of the SSM/T-2 data into reanalysis, which generally applies
811 bias corrections to such data when assimilating them. However, this does require further
812 attention, to enable, for example, direct use of the data to retrieve humidity information, unless
813 applying a priori approaches such as harmonization (e.g., Giering et al., 2019).

814 Finally, Figure 13 shows that the increase in observation horizontal local variability is
815 associated with a slow but steady decrease of the bias towards negative values in the departures.
816 This effect is most pronounced for the lowest-peaking channel in Figure 13(c), and consistent
817 with the findings of Calbet et al. (2018).

818 In summary, our simulation results indicate that the information about uncertainty and
819 observation horizontal local variability should be of interest for users of the SSM/T-2 data
820 interested, for example, in clear-sky humidity retrievals.

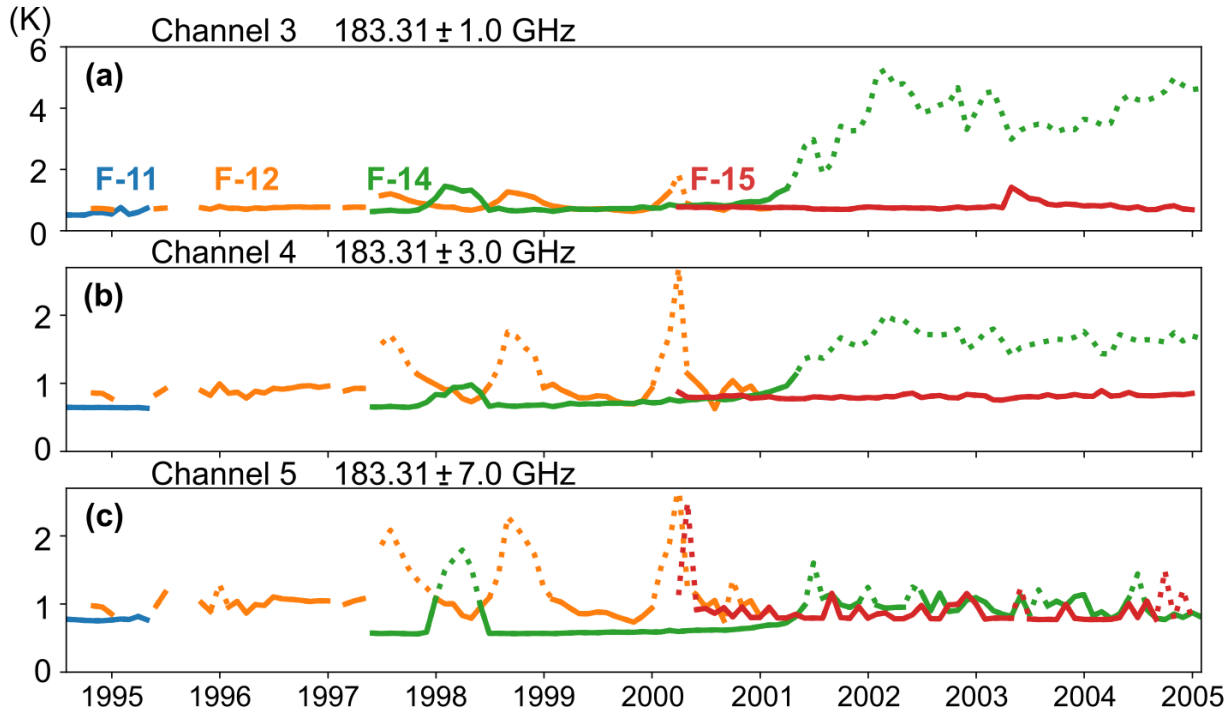

Figure 12. Total uncertainty (monthly mean) associated with the SSM/T-2 antenna temperatures, as a function of time, for the three 183.31 GHz channels, ordered from highest-peaking (a) to lowest-peaking (c), for all satellites (F-11, F-12, F-14, F-15, see colored labels). Dots indicate time periods excluded in subsequent data analysis because the uncertainty estimate exceeds twice the pre-launch NEDT specification.

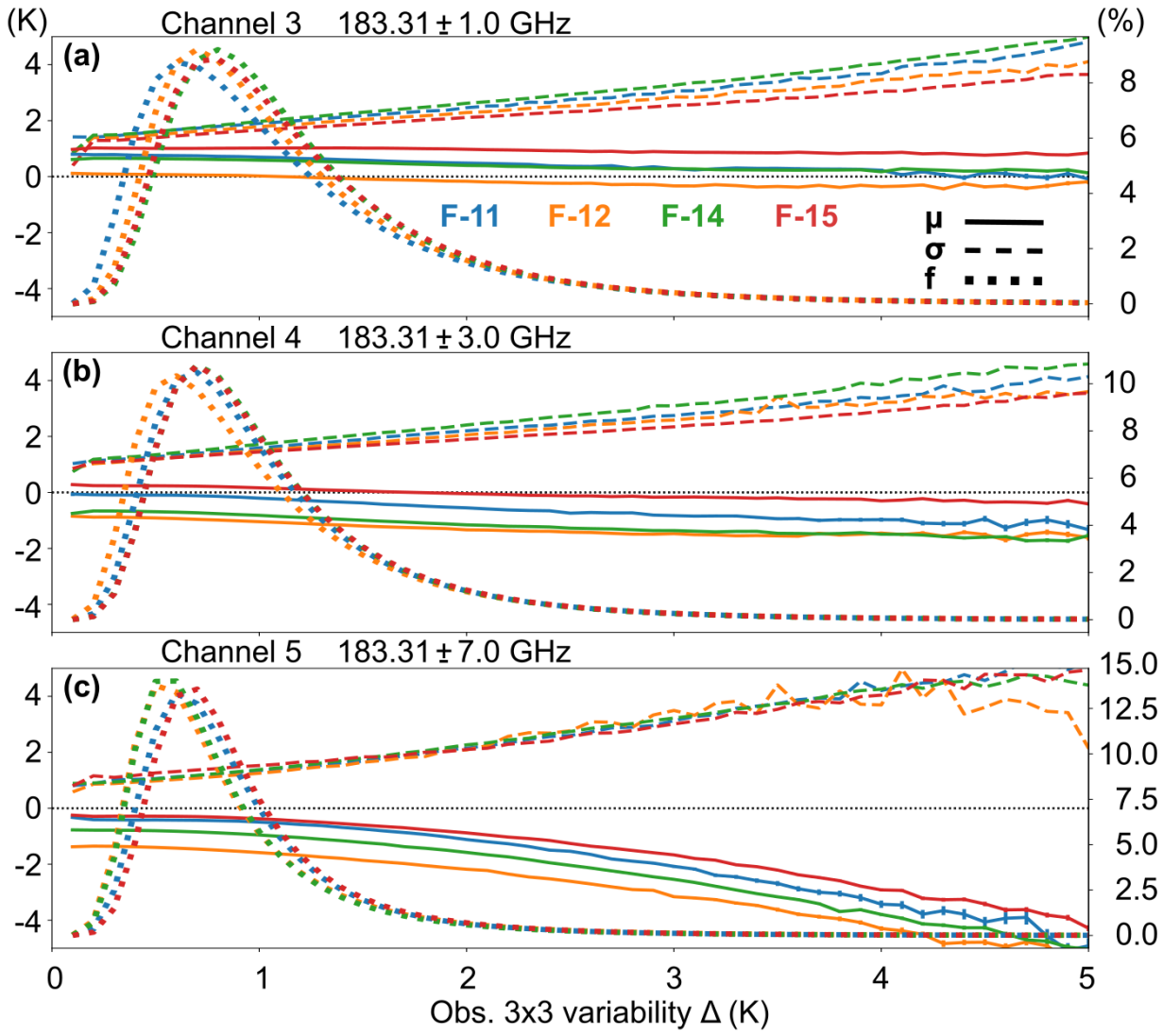

Figure 13. For the three SSM/T-2 183.31 GHz channels, (a) to (c), mean (μ, solid lines) and standard deviation (σ, dashed lines) of departures (in K, left-hand-side vertical axis), as a function of the observation horizontal local variability (Δ, horizontal axis, in bins of 0.1 K), with dotted lines showing the data distribution (f, normalized in percent, right-hand-side vertical axis).

6 Discussion

There are several factors that could explain the departures between instrument data records and simulations from reanalyses reported and analyzed in this paper.

First, there is the issue of data independence. One needs to assess, for each comparison, if the observational data record was assimilated in the reanalysis that is used for the simulations. The data of several data records used in this paper were independent (SI-1, SSM/T-2, MRIR). Other data were partly or indirectly used in the reanalysis. As for example is the case for the MVIRI radiances, which were indirectly assimilated as another variable or derived product (such as atmospheric motion vector, or to construct the sea-ice or sea-surface temperature that was used as forcing in reanalysis). The HIRS data, on the other hand, were fully assimilated.

However, our analysis only considers the low-frequency variability of departures. This variability is known to remain distinct between reanalysis and the assimilated data, thanks to the mechanism of the variational bias correction, even if the possibility of aliasing the signals cannot be ruled out completely.

Second, there are changes in reanalysis quality over time. These may be due to general improvement of the observing system (e.g., Dee et al., 2011), or related to instances of degraded performance owing to suboptimal data use or more challenging natural variability, insufficiently observed, or suboptimal data use. When such changes occur, they will affect all comparisons, to all sensors, making it easier to identify whether or not the problem stems from the reanalysis or the satellite data record.

Third, even if different reanalyses (such as ERA5 and ERA-Interim) are from different generations, they often used very similar observations input (especially in the early years). This limits the degree of independence between comparisons to several reanalyses. For this reason, global reanalyses from a wider diversity of producers should be selected in future work.

Fourth, there are instrument-induced effects that are not all understood or simulated. A few of these effects are listed by Fennig et al. (2017), for example, for the Nimbus-7 SMMR data record. These effects include unknown variations in the satellite zenith angle, errors in the satellite attitude control, potential errors in the underlying level 1B processing and, more generally, insufficient correction of instrument-induced effects (such as calibration, spill-over, and polarization mixing). These are all effects that are best addressed at the source, and for which the simulations can help quantifying the overall cumulated effects. Even in cases where instrument errors cannot be corrected at the source, such as the case of the MRIR data record, improvements in bias correction predictors will help in including early satellite data into either data assimilation systems, or at least in its use as a check on aspects of a reanalysis for periods with limited or no satellite data.

Fifth, the quality of radiance simulations to reproduce the variability in the observations is not equal for all channels/instruments. This originates in the spatio-temporal scale and magnitude of natural phenomena responsible for the variability, differing by instrument and channel, as compared to instrument and simulation resolutions and uncertainties. One may cite as an example MVIRI, an instrument whose IFOV (see Table 1) is much smaller than the horizontal resolution of global reanalyses. The simulation of the MVIRI infrared window channel generally performs better over ocean than land, but on the other hand, the simulation of the MVIRI water vapor channel features larger spreads in departures than those of the window channels, owing to the upper-air water vapor coarse-resolution and corresponding variability representation in the reanalyses. Another example is when a satellite data record contains signals that originate from changes not contained in the simulations, such as volcanic aerosols (AVHRR) or possible changes in trace gases whose concentrations have evolved due to industrial emissions (SI-1). All these cases can be summed up by the issue of representativeness uncertainty between observations and reanalysis.

Overall, the general approach followed here can be summarized by three principles: (a) “all else being equal, an improved reprocessing should lead to an improved fit of the observed data to simulations”, and so should also (b) an improved simulation setup, and (c) an improved reanalysis. While this work is not a proof of these principles, we note that we have not found examples to the contrary in our investigations. However, one must remember that, under special

887 circumstances, the situation of two observations and simulations agreeing for the wrong reason
888 cannot be ruled out (e.g., Joiner et al., 2004). To reduce the chances of such mishap, we
889 emphasize that the comparisons as shown here should, as much as possible, draw on a large
890 number of data samples.

891 Another important element to consider, when analyzing departures between observations
892 and simulations, are the quality controls (Supplement Text S1). They may appear as trivial to
893 some readers, but far less obvious to others. While it should normally suffice to read the
894 documentation that accompanies every data record, and then to apply the quality flags suggested
895 by the documentation after reading the data, our experience suggests that more should be done in
896 the future to ease the application of quality flags. The aim should be to preserve the flexibility for
897 expert users but also to guide less-expert users and leave less room to interpretation.

898 Finally, an issue encountered during the course of this work was that each climate data
899 record tends to adopt a data representation that is contemporary to the time of the mission,
900 reflecting in general the data transmission constraints imposed by radio transmission bandwidth
901 and digitization. This is no different to practices followed to disseminate in-situ observation data.
902 However, if one priority is to improve inter-operability of datasets for comparisons and other
903 applications, the multitude of data models to represent observations is a barrier to integration.
904 Indeed, it requires, in each case, to adapt computer code. To circumvent this issue, initiatives
905 have been proposed, to promote a single data model (Nativi et al., 2008). Such initiatives will
906 greatly simplify the data integration and data comparisons, for example with other observations
907 or with models, possibly via simulations as shown here.

908 **7 Conclusions**

909 This paper applies radiance simulators to the Fundamental (Climate) Data Records
910 (F(C)DRs of several satellite instruments, using as input global climate reanalyses. While the
911 methodology of radiance simulators is not new, we demonstrate that their application enables
912 three classes of applications.

913 In the first class of applications, assumptions about a data record organization (order of
914 channels), its quality, or data corrections, may be verified. For this, we mostly draw from
915 examples where the data have been characterized long ago, such as the MVIRI and HIRS data
916 records, and much progress has been made since then. We use examples where the
917 methodological advance of reprocessing is on a level that benefits from a high-quality a priori
918 comparison to validate the impact, such as identifying image anomalies in geostationary images
919 or improving the coherence between data records and reanalyses with modern cloud masks.

920 Regarding the volcanic eruption of Mount Pinatubo, we find a cooling on the order of 1
921 K for brightness temperatures from AVHRR and HIRS window channels (short-wave and long-
922 wave alike), with concomitant increase in reflectance for the AVHRR near-infrared channel of a
923 few percent. We also revisit how fast the atmospheric effects of the eruption propagated away
924 from the Tropics. In line with previous findings, we confirm differences in the timing of peak
925 radiative effects of several months between the Mediterranean and the Southern Oceans as
926 compared to the Tropics, where the volcanic eruption had taken place.

927 In the second class of applications, coherence between global datasets of different natures
928 can be assessed. The high spectral resolution data collected by the SI-1 instrument allows
929 confirmation of improvements in the quality of the latest Japanese global reanalysis, JRA-3Q, for

stratospheric ozone. Spectral spikes in departures, observed for all reanalyses, also suggest that several trace gases' (in particular halocarbons) concentrations assumed in the radiative transfer may differ from actual concentrations in 1979. Furthermore, we present first estimates of SI-1 random uncertainty, assuming independence of random uncertainty between the sources of error. Given such caveats, our findings suggest the combined instrument noise and radiative transfer random uncertainties increase in the far-infrared region. In this respect, observations from the future FORUM instrument will be useful to enhance general experience and understanding of the performance of radiative transfer models in the far-infrared. At higher wavenumbers (600—1200 cm^{-1}), we find combined SI-1 instrument noise equivalent delta temperature (NEDT) and representativeness uncertainties at 280 K to be generally in the range 0.8—1.0 K.

Another example shown, with MRIR, illustrates how differences, which could be interpreted as incoherencies between reanalyses and observations, can be differently reduced numerically, depending on the set of bias predictors chosen. While this can minimize systematic differences, another importance of this approach is to gain understanding about the potential sources of errors in the satellite data. This ties the present study to a third class of applications: informing users on key characteristics of a data record.

In this third class of applications, we show cases of simulations of, and comparisons with, data records from SMMR, SSM/T-2, and Meteosat second-generation. For SMMR, the findings are that the existing data records suffer for the horizontally-polarized 21 GHz channel from large oscillating biases, and that all channels exhibit a different behavior after a Special Observing Period in 1986. Given the value of the SMMR data in bridging with the SSM/I data record, this calls to consider a potential new reprocessing of the SMMR data record from the original data.

For SSM/T-2, we find that uncertainty information and horizontal local variability in the observations make a large difference to improve the agreement between reanalysis and clear-sky simulations. This suggests that these parameters would need to be taken into account in applications, such as clear-sky humidity retrievals.

For Meteosat Second Generation, we find that the variability of the satellite position around its nominal position has most likely left a signature in the data record. For climate applications, such changes in position are needed to take into account or else they may get aliased into regional patterns of changes in the downstream products.

For all cases of the third class of applications, the results do not constitute final conclusions, but, instead, provide information for users and applications to take into account.

In all the examples shown in the study, the effort consists in bringing all the sources of information into the same observation space (times, locations, instrument channel, and viewing geometry), after having applied quality controls following the data records' user documentation. Notwithstanding the particular issue posed by the diversity of observation data models, this approach, if generalized and made more systematic, would aid tracking of progress in climate reanalyses and satellite climate data records alike. This would help to accelerate the delivery of high-quality climate data records to serve climate services. The prospects for such an activity are not identified specifically in the GCOS Implementation Plan (World Meteorological Organization (WMO) et al., 2022). However, this plan identifies an action to co-locate in-situ and satellite measurements. The present paper demonstrates that there may be great benefits in considering also state-of-the-art reanalyses in such co-locations.

973 The data records discussed in this paper are mostly limited to the representation of
974 atmospheric phenomena and corresponding satellite observations. In parallel, today's Earth
975 system models are developed to encompass more components, including anthropogenic effects.
976 One may thus expect the same methods as presented here to be applicable to support the
977 development of data records related to other observables that impact our environment, such as
978 human activity and biodiversity. These two fields are of utmost importance, provided that
979 physical methods are developed to relate these fields to satellite measurements via simulators.
980 For both fields, there have already been key developments (e.g., Gao et al., 2015; Schweiger &
981 Laliberté, 2022, respectively). The methods set forth in the present paper may serve to continue
982 progress in these areas and to support advances in long data records and corresponding models
983 that describe human activity and biodiversity.

984 Thirty years after the 1992 Earth Summit, it is worth remembering that its participants
985 had identified three topics to be tackled within regular meetings of Conventions Of the Parties
986 (COP), i.e., climate change, biodiversity collapse, and desertification. Today, these three topics
987 appear to be on a collision course, notwithstanding increasing demands for resources from a
988 growing world population. This calls for more urgent action to understand the inter-relations
989 between all these application areas, through better exploitation of environmental measurements,
990 models, and reanalyses, which integrate the most diverse sources of data for our environment.

991 **Acknowledgments**

992 This work benefited from strong inter-agency collaboration, noting support from the European
993 Union Copernicus Climate Change Service (C3S) and the institutions to which the authors are
994 affiliated. The EUMETSAT NWP-SAF is thanked for adding support to several instruments,
995 with special thanks to Emma Turner and James Hocking. The EUMETSAT CM-SAF is
996 acknowledged for providing data records used in this work, and specials thanks are addressed to
997 Karl-Göran Karlsson, Abhay Devasthale, Martin Raspaud, Diana Stein, Nathalie Selbach,
998 Stephan Finkensieper, Karsten Fennig, Marc Schröder, and Rainer Hollmann. The authors wish
999 to thank NOAA for the SSM/T-2 Sensor Data Record. The authors also wish to thank librarians
1000 at EUMETSAT, NASA, and NOAA for help locating early satellite instruments' technical
1001 documentation.

1002 **Open Research**

1003 The satellite datasets analyzed in this study are available as follows: MVIRI (EUMETSAT, 2020):
1004 doi:10.15770/EUM_SEC_CLM_0009, SEVIRI (EUMETSAT, 2015):

doi:10.15770/EUM_SEC_CLM_0008, MRIR (McCulloch, 2014): doi:10.5067/XTJ53AK84QRL, SI-1 (Poli et al., 2023): doi:10.5281/zenodo.7912742, HIRS (EUMETSAT, 2022): doi:10.15770/EUM_SEC_CLM_0026, AVHRR (EUMETSAT, 2023): doi:10.15770/EUM_SEC_CLM_0060, SMMR (Fennig et al., 2017): doi:10.5676/EUM_SAF_CM/FCDR_MWI/V003, SSM/T-2 (EUMETSAT, 2021): doi:10.15770/EUM_SEC_CLM_0050, and CLARA-A3 cloud mask (Karlsson et al., 2023): doi:10.5676/EUM_SAF_CM/CLARA_AVHRR/V003. The reanalysis datasets are available as follows: ERA5 (Copernicus Climate Change Service, 2018): doi:10.24381/cds.bd0915c6, ERA-20C (ECMWF, 2014): doi:10.5065/D6VQ30QG, ERA-Interim (ECMWF, 2009): doi:10.5065/D6CR5RD9, JRA-55 (Japan Meteorological Agency, 2013): https://search.diasjp.net/en/dataset/JRA55, and JRA-3Q (Japan Meteorological Agency, 2022): https://search.diasjp.net/en/dataset/JRA3Q. The radiance simulator used in this study is RADSIM (EUMETSAT NWP-SAF, 2021), available from https://nwp-saf.eumetsat.int/site/software/radiance-simulator/. We used RADSIM version 3.0. The radiative transfer model used in this study is RTTOV (EUMETSAT NWP-SAF, 2020), available from: https://nwp-saf.eumetsat.int/site/software/rttov/. We used RTTOV version v13.0 except for simulating MRIR, where RTTOV v12.2 was used.

References

Aires, F., Rossow, W. B., & Chédin, A. (2002). Rotation of EOFs by the Independent Component Analysis: Toward a Solution of the Mixing Problem in the Decomposition of Geophysical Time Series. *Journal of the Atmospheric Sciences*, *59*(1), 111–123. https://doi.org/10.1175/1520-0469(2002)059<0111:ROEBTI>2.0.CO;2

Andersson, A., Graw, K., Schröder, M., Fennig, K., Liman, J., Bakan, S., et al. (2017). Hamburg Ocean Atmosphere Parameters and Fluxes from Satellite Data - HOAPS 4.0 [NetCDF v4]. Satellite Application Facility on Climate Monitoring (CM SAF). https://doi.org/10.5676/EUM_SAF_CM/HOAPS/V002

Barbosa, H. A., Lakshmi Kumar, T. V., Paredes, F., Elliott, S., & Ayuga, J. G. (2019). Assessment of Caatinga response to drought using Meteosat-SEVIRI Normalized Difference Vegetation Index (2008–2016). *ISPRS*

Journal of Photogrammetry and Remote Sensing, *148*, 235–252. https://doi.org/10.1016/j.isprsjprs.2018.12.014

Bell, B., Hersbach, H., Simmons, A., Berrisford, P., Dahlgren, P., Horányi, A., et al. (2021). The ERA5 global reanalysis: Preliminary extension to 1950. *Quarterly Journal of the Royal Meteorological Society*, *147*(741), 4186–4227. https://doi.org/10.1002/qj.4174

Bell, W., Di Michele, S., Bauer, P., McNally, T., English, S. J., Atkinson, N., et al. (2010). The Radiometric Sensitivity Requirements for Satellite Microwave Temperature Sounding Instruments for Numerical Weather Prediction. *Journal of Atmospheric and Oceanic Technology*, *27*(3), 443–456. https://doi.org/10.1175/2009JTECHA1293.1

Brasseur, G. P., & Gallardo, L. (2016). Climate services: Lessons learned and future prospects. *Earth's Future*, *4*, 79–89. https://doi.org/10.1002/2015EF000338

Brindley, H. E., & Bantges, R. J. (2016). The Spectral Signature of Recent Climate Change. *Current Climate Change Reports*, *2*(3), 112–126. https://doi.org/10.1007/s40641-016-0039-5

Buehler, S. A., Kuvatov, M., & John, V. O. (2005). Scan asymmetries in AMSU-B data. *Geophysical Research Letters*, *32*(24), L24810. https://doi.org/10.1029/2005GL024747

Calbet, X., Peinado-Galan, N., DeSouza-Machado, S., Kursinski, E. R., Oria, P., Ward, D., et al. (2018). Can turbulence within the field of view cause significant biases in radiative transfer modeling at the 183 GHz band? *Atmospheric Measurement Techniques*, *11*(12), 6409–6417. https://doi.org/10.5194/amt-11-6409-2018

Copernicus Climate Change Service. (2018). ERA5 [Data set]. Copernicus Climate Change Service (C3S) Data Store. https://doi.org/10.24381/cds.bd0915c6

Dai, L., Che, T., & Ding, Y. (2015). Inter-Calibrating SMMR, SSM/I and SSMI/S Data to Improve the Consistency of Snow-Depth Products in China. *Remote Sensing*, *7*(6), 7212–7230. https://doi.org/10.3390/rs70607212

De Jong, E. (1978). Space Age Computing. *Physics Bulletin*, *29*(10), 459–462. https://doi.org/10.1088/0031-9112/29/10/017

De Vrese, P., & Hagemann, S. (2018). Uncertainties in modelling the climate impact of irrigation. *Climate Dynamics*, *51*(5–6), 2023–2038. https://doi.org/10.1007/s00382-017-3996-z

1058 Dee, D. P., & Uppala, S. (2009). Variational bias correction of satellite radiance data in the ERA-Interim reanalysis.
1059 *Quarterly Journal of the Royal Meteorological Society*, *135*(644), 1830–1841.
1060 https://doi.org/10.1002/qj.493
1061 Dee, D. P., Uppala, S. M., Simmons, A. J., Berrisford, P., Poli, P., Kobayashi, S., et al. (2011). The ERA-Interim
1062 reanalysis: configuration and performance of the data assimilation system. *Quarterly Journal of the Royal*
1063 *Meteorological Society*, *137*(656), 553–597. https://doi.org/10.1002/qj.828
1064 Desroziers, G., Berre, L., Chapnik, B., & Poli, P. (2005). Diagnosis of observation, background and analysis-error
1065 statistics in observation space. *Quarterly Journal of the Royal Meteorological Society*, *131*(613), 3385–
1066 3396. https://doi.org/10.1256/qj.05.108
1067 Doutriaux-Boucher, M., Pelon, J., Trouillet, V., Sèze, G., Le Treut, H., Flamant, P., & Desbois, M. (1998).
1068 Simulation of satellite lidar and radiometer retrievals of a general circulation model three-dimensional
1069 cloud data set. *Journal of Geophysical Research: Atmospheres*, *103*(D20), 26025–26039.
1070 https://doi.org/10.1029/98JD02378
1071 ECMWF. (2009). ERA-Interim [Data set]. UCAR/NCAR - Research Data Archive.
1072 https://doi.org/10.5065/D6CR5RD9
1073 ECMWF. (2014). ERA-20C Project: ECMWF Atmospheric Reanalysis of the 20th Century [Data set].
1074 UCAR/NCAR - Research Data Archive. https://doi.org/10.5065/D6VQ30QG
1075 EUMETSAT. (2015). All-Sky Radiances - MSG - 0 degree (CF-015 Release 1) [Data set]. European Organisation
1076 for the Exploitation of Meteorological Satellites Data Store.
1077 https://doi.org/10.15770/EUM_SEC_CLM_0008
1078 EUMETSAT. (2020). MVIRI Level 1.5 Climate Data Record Release 1 - MFG - 0 degree [Data set]. European
1079 Organisation for the Exploitation of Meteorological Satellites Data Store.
1080 https://doi.org/10.15770/EUM_SEC_CLM_0009
1081 EUMETSAT. (2021). SSM/T-2 Microwave Humidity Sounder Climate Data Record Release 2 - DMSP (Version 2)
1082 [Data set]. European Organisation for the Exploitation of Meteorological Satellites Data Store.
1083 https://doi.org/10.15770/EUM_SEC_CLM_0050

1084 EUMETSAT. (2022). HIRS Level 1C Fundamental Data Record Release 1 - Multimission - Global [Data set].
1085 European Organisation for the Exploitation of Meteorological Satellites Data Store.
1086 https://doi.org/10.15770/EUM_SEC_CLM_0026
1087 EUMETSAT. (2023). AVHRR Fundamental Data Record - Release 1 - Multimission [Data set]. European
1088 Organisation for the Exploitation of Meteorological Satellites Data Store.
1089 https://doi.org/10.15770/EUM_SEC_CLM_0060
1090 EUMETSAT NWP-SAF. (2020). Radiative Transfer for TOVS (RTTOV) [Software] (Version 13.0). Retrieved
1091 from https://nwp-saf.eumetsat.int/site/software/rttov/download/
1092 EUMETSAT NWP-SAF. (2021). Radiance Simulator (RADSIM) [Software] (Version 3.0). Retrieved from
1093 https://nwp-saf.eumetsat.int/site/software/radiance-simulator/download/
1094 Fennig, K., Schröder, M., & Hollmann, R. (2017). Fundamental Climate Data Record of Microwave Imager
1095 Radiances, Edition 3 [Data set]. Satellite Application Facility on Climate Monitoring (CM SAF).
1096 https://doi.org/10.5676/EUM_SAF_CM/FCDR_MWI/V003
1097 Gao, B., Huang, Q., He, C., & Ma, Q. (2015). Dynamics of Urbanization Levels in China from 1992 to 2012:
1098 Perspective from DMSP/OLS Nighttime Light Data. *Remote Sensing*, *7*(2), 1721–1735.
1099 https://doi.org/10.3390/rs70201721
1100 Gibson, J., Kållberg, P. W., Uppala, S., Hernandez, A., Nomura, A., & Serrano, E. (1997). *ERA Description* (ERA
1101 Report No. 1). Reading, United Kingdom: ECMWF. Retrieved from
1102 https://www.ecmwf.int/en/elibrary/74605-era-description
1103 Giering, R., Quast, R., Mittaz, J. P. D., Hunt, S. E., Harris, P. M., Woolliams, E. R., & Merchant, C. J. (2019). A
1104 Novel Framework to Harmonise Satellite Data Series for Climate Applications. *Remote Sensing*, *11*(9),
1105 1002. https://doi.org/10.3390/rs11091002
1106 Gordon, A. H. (1962). Satellite Meteorology. *Nature*, *195*(4847), 1161–1162. https://doi.org/10.1038/1951161a0
1107 Hanel, R. A., Schlachman, B., Clark, F. D., Prokesh, C. H., Taylor, J. B., Wilson, W. M., & Chaney, L. (1970). The
1108 Nimbus III Michelson Interferometer. *Applied Optics*, *9*(8), 1767. https://doi.org/10.1364/AO.9.001767
1109 Hanel, R. A., Conrath, B. J., Kunde, V. G., Prabhakara, C., Revah, I., Salomonson, V. V., & Wolford, G. (1972).
1110 The Nimbus 4 infrared spectroscopy experiment: 1. Calibrated thermal emission spectra. *Journal of*
1111 *Geophysical Research*, *77*(15), 2629–2641. https://doi.org/10.1029/JC077i015p02629

1112 Hans, I., Burgdorf, M., John, V. O., Mittaz, J., & Buehler, S. A. (2017). Noise performance of microwave humidity
1113 sounders over their lifetime. *Atmospheric Measurement Techniques*, *10*(12), 4927–4945.
1114 https://doi.org/10.5194/amt-10-4927-2017
1115 Harrison, C. T., Washington, R., & Engelstaedter, S. (2019). A 14-Year Climatology of Saharan Dust Emission
1116 Mechanisms Inferred From Automatically Tracked Plumes. *Journal of Geophysical Research:*
1117 *Atmospheres*, *124*(16), 9665–9690. https://doi.org/10.1029/2019JD030291
1118 Harrison, J. J. (2018). New and improved infrared absorption cross sections for trichlorofluoromethane (CFC-11).
1119 *Atmospheric Measurement Techniques*, *11*(10), 5827–5836. https://doi.org/10.5194/amt-11-5827-2018
1120 Hasselmann, K. (1997). Multi-pattern fingerprint method for detection and attribution of climate change. *Climate*
1121 *Dynamics*, *13*(9), 601–611. https://doi.org/10.1007/s003820050185
1122 Hersbach, H., Bell, B., Berrisford, P., Hirahara, S., Horányi, A., Muñoz-Sabater, J., et al. (2020). The ERA5 global
1123 reanalysis. *Quarterly Journal of the Royal Meteorological Society*, *146*(730), 1999–2049.
1124 https://doi.org/10.1002/qj.3803
1125 Hocking, J. (2022). *Radiance Simulator v3.1 User Guide* (No. NWPSAF-MO-UD-051). EUMETSAT NWP-SAF.
1126 Retrieved from https://nwp-
1127 saf.eumetsat.int/site/download/documentation/rad_sim/user_documentation/RadSim_UserGuide.pdf
1128 Houborg, R., & McCabe, M. F. (2016). Adapting a regularized canopy reflectance model (REGFLEC) for the
1129 retrieval challenges of dryland agricultural systems. *Remote Sensing of Environment*, *186*, 105–120.
1130 https://doi.org/10.1016/j.rse.2016.08.017
1131 Hubert, S., & Swale, J. (1984). Stationkeeping of a constellation of geostationary communications satellites. In
1132 *Astrodynamics Conference*. Seattle,WA,U.S.A.: American Institute of Aeronautics and Astronautics.
1133 https://doi.org/10.2514/6.1984-2042
1134 Hunt, G. E., & Grant, I. P. (1969). Discrete Space Theory of Radiative Transfer and its Application to Problems in
1135 Planetary Atmospheres. *Journal of the Atmospheric Sciences*, *26*(5), 963–972.
1136 https://doi.org/10.1175/1520-0469(1969)026<0963:DSTORT>2.0.CO;2
1137 Iturbide, M., Gutiérrez, J. M., Alves, L. M., Bedia, J., Cerezo-Mota, R., Cimadevilla, E., et al. (2020). An update of
1138 IPCC climate reference regions for subcontinental analysis of climate model data: definition and

aggregated datasets. *Earth System Science Data*, *12*(4), 2959–2970. https://doi.org/10.5194/essd-12-2959-2020

Jackson, D. L., & Soden, B. J. (2007). Detection and Correction of Diurnal Sampling Bias in HIRS/2 Brightness Temperatures. *Journal of Atmospheric and Oceanic Technology*, *24*(8), 1425–1438. https://doi.org/10.1175/JTECH2062.1

Japan Meteorological Agency. (2013). The Japanese 55-year Reanalysis (JRA-55) [Data set]. Japan Agency for Marine-Earth Science and Technology Data Integration and Analysis System (DIAS). Retrieved from https://search.diasjp.net/en/dataset/JRA55

Japan Meteorological Agency. (2022). The Japanese Reanalysis for Three Quarters of a Century (JRA-3Q) [Data set]. Japan Agency for Marine-Earth Science and Technology Data Integration and Analysis System (DIAS). Retrieved from https://search.diasjp.net/en/dataset/JRA3Q

John, V. O., & Buehler, S. A. (2004). The impact of ozone lines on AMSU-B radiances. *Geophysical Research Letters*, *31*, L21108. https://doi.org/10.1029/2004GL021214

Joiner, J., & Poli, P. (2005). Note on the effect of horizontal gradients for nadir-viewing microwave and infrared sounders. *Quarterly Journal of the Royal Meteorological Society*, *131*(608), 1783–1792. https://doi.org/10.1256/qj.04.125

Joiner, J., & Rokke, L. (2000). Variational cloud-clearing with TOVS data. *Quarterly Journal of the Royal Meteorological Society*, *126*(563), 725–748. https://doi.org/10.1002/qj.49712656316

Joiner, J., Poli, P., Frank, D., & Liu, H. C. (2004). Detection of cloud-affected AIRS channels using an adjacent-pixel approach. *Quarterly Journal of the Royal Meteorological Society*, *130*(599), 1469–1487. https://doi.org/10.1256/qj.03.93

Karlsson, Karl-Göran, Riihelä, Aku, Trentmann, Jörg, Stengel, Martin, Solodovnik, Irina, Meirink, Jan Fokke, et al. (2023). CLARA-A3: CM SAF cLoud, Albedo and surface RAdiation dataset from AVHRR data - Edition 3 (Version 3.0) [Data set]. Satellite Application Facility on Climate Monitoring (CM SAF). https://doi.org/10.5676/EUM_SAF_CM/CLARA_AVHRR/V003

Kempe, V. (1980). Satellite-Fourier-spectrometer for Meteor-25: design problems and mission. *Acta Astronautica*, *7*(7), 893–902. https://doi.org/10.1016/0094-5765(80)90078-8

1166 Kempe, V., Oertel, D., Schuster, R., Becker-Ross, H., & Jahn, H. (1980). Absolute IR-spectra from the measurement
1167 of Fourier-spectrometers aboard Meteor 25 and 28. *Acta Astronautica*, *7*(12), 1403–1416.
1168 https://doi.org/10.1016/0094-5765(80)90015-6
1169 King, O., & Dudhia, A. (2017). Atmospheric Infrared Spectrum Atlas: Zenith Sky Optical Thickness Infrared
1170 Spectrum. Retrieved May 16, 2023, from http://eodg.atm.ox.ac.uk/ATLAS/zenith-absorption
1171 Kobayashi, S., Kosaka, Y., Chiba, J., Tokuhiro, T., Harada, Y., Kobayashi, C., & Naoe, H. (2021). JRA-3Q:
1172 Japanese Reanalysis for Three Quarters of a Century. Presented at the Joint WCRP-WWRP Symposium on
1173 Data Assimilation and Reanalysis/ECMWF Annual Seminar 2021, Online. Retrieved from https://symp-
1174 bonn2021.sciencesconf.org/data/355900.pdf
1175 Kobayashi, Shinya, Ota, Y., Harada, Y., Ebita, A., Moriya, M., Onoda, H., et al. (2015). The JRA-55 Reanalysis:
1176 General Specifications and Basic Characteristics. *Journal of the Meteorological Society of Japan. Ser. II*,
1177 *93*(1), 5–48. https://doi.org/10.2151/jmsj.2015-001
1178 Krzeminski, B., Bormann, N., Kelly, G., McNally, T., & Bauer, P. (2009). *Revision of the HIRS cloud detection at*
1179 *ECMWF* (EUMETSAT/ECMWF Fellowship Prog. Res. Rep. No. 19). Reading, United Kingdom:
1180 ECMWF. Retrieved from https://www.ecmwf.int/sites/default/files/elibrary/2009/10561-revision-hirs-
1181 cloud-detection-ecmwf.pdf
1182 Liefhebber, F., Lammens, S., Brussee, P. W. G., Bos, A., John, V. O., Rüthrich, F., et al. (2020). Automatic quality
1183 control of the Meteosat First Generation measurements. *Atmospheric Measurement Techniques*, *13*(3),
1184 1167–1179. https://doi.org/10.5194/amt-13-1167-2020
1185 Lu, Q., & Bell, W. (2014). Characterizing Channel Center Frequencies in AMSU-A and MSU Microwave Sounding
1186 Instruments. *Journal of Atmospheric and Oceanic Technology*, *31*(8), 1713–1732.
1187 https://doi.org/10.1175/JTECH-D-13-00136.1
1188 Mahon, R., Greene, C., Cox, S.-A., Guido, Z., Gerlak, A. K., Petrie, J.-A., et al. (2019). Fit for purpose?
1189 Transforming National Meteorological and Hydrological Services into National Climate Service Centers.
1190 *Climate Services*, *13*, 14–23. https://doi.org/10.1016/j.cliser.2019.01.002
1191 Masson-Delmotte, V., Zhai, P., Pirani, A., Connors, S. L., Péan, C., Berger, S., et al. (Eds.). (2021). *Climate Change*
1192 *2021: The Physical Science Basis. Contribution of Working Group I to the Sixth Assessment Report of the*

1193 *Intergovernmental Panel on Climate Change*. Cambridge, United Kingdom and New York, NY, USA:
1194 Cambridge University Press. https://doi.org/10.1017/9781009157896
1195 McCulloch, A. (2014). MRIR/Nimbus-3 Level 1 Meteorological Radiation Data V001 [Data set]. NASA Goddard
1196 Earth Sciences Data and Information Services Center (GES DISC). https://doi.org/10.5067/xtj53ak84qrl
1197 Mears, C. A., & Wentz, F. J. (2017). A Satellite-Derived Lower-Tropospheric Atmospheric Temperature Dataset
1198 Using an Optimized Adjustment for Diurnal Effects. *Journal of Climate*, *30*(19), 7695–7718.
1199 https://doi.org/10.1175/JCLI-D-16-0768.1
1200 Mitchell, T. M. (1997). *Machine Learning*. New York: McGraw-Hill.
1201 Munro, R., Lang, R., Klaes, D., Poli, G., Retscher, C., Lindstrot, R., et al. (2016). The GOME-2 instrument on the
1202 Metop series of satellites: instrument design, calibration, and level 1 data processing – an overview.
1203 *Atmospheric Measurement Techniques*, *9*(3), 1279–1301. https://doi.org/10.5194/amt-9-1279-2016
1204 National Research Council (U.S.) (Ed.). (2004). *Climate data records from environmental satellites*. Washington,
1205 D.C: National Academies Press.
1206 Nativi, S., Caron, J., Domenico, B., & Bigagli, L. (2008). Unidata's Common Data Model mapping to the ISO
1207 19123 Data Model. *Earth Science Informatics*, *1*(2), 59–78. https://doi.org/10.1007/s12145-008-0011-6
1208 Newman, S., Carminati, F., Lawrence, H., Bormann, N., Salonen, K., & Bell, W. (2020). Assessment of New
1209 Satellite Missions within the Framework of Numerical Weather Prediction. *Remote Sensing*, *12*(10), 1580.
1210 https://doi.org/10.3390/rs12101580
1211 Njoku, E. (2003). Nimbus-7 SMMR Pathfinder Brightness Temperatures, Version 1 [Data set]. NASA National
1212 Snow and Ice Data Center DAAC. https://doi.org/10.5067/7Y1XWXT07HH8
1213 Oertel, D., Spänkuch, D., Jahn, H., Becker-Ross, H., Stadthaus, W., Nopirakowski, J., et al. (1985). Infrared
1214 spectrometry of Venus from "Venera-15" and "Venera-16." *Advances in Space Research*, *5*(9), 25–36.
1215 https://doi.org/10.1016/0273-1177(85)90267-4
1216 Pachot, C., Carnicero Domínguez, B., Sierk, B., Mariani, F., Riel, S., Oetjen, H., et al. (2021). Far infrared Fourier
1217 transform spectrometer breadboard activities for the FORUM mission, ESA's 9th Earth Explorer. In Z.
1218 Sodnik, B. Cugny, & N. Karafolas (Eds.), *International Conference on Space Optics — ICSO 2020* (p. 75).
1219 Online Only, France: SPIE. https://doi.org/10.1117/12.2599355

1220 Parker, H. R., Cornforth, R. J., Boyd, E., James, R., Otto, F. E. L., & Allen, M. R. (2015). Implications of event
1221 attribution for loss and damage policy. *Weather*, *70*(9), 268–273. https://doi.org/10.1002/wea.2542
1222 Poli, P., Hersbach, H., Dee, D. P., Berrisford, P., Simmons, A. J., Vitart, F., et al. (2016). ERA-20C: An
1223 Atmospheric Reanalysis of the Twentieth Century. *Journal of Climate*, *29*(11), 4083–4097.
1224 https://doi.org/10.1175/JCLI-D-15-0556.1
1225 Poli, P., Dee, D. P., Saunders, R., John, V. O., Rayer, P., Schulz, J., et al. (2017). Recent Advances in Satellite Data
1226 Rescue. *Bulletin of the American Meteorological Society*, *98*(7), 1471–1484.
1227 https://doi.org/10.1175/BAMS-D-15-00194.1
1228 Poli, P., Hanschmann, T., Roebeling, R., Schulz, J., John, V., Théodore, B., et al. (2023). Brightness Temperature
1229 Spectra 400-1200 cm**-1 from satellite METEOR-29 instrument SI-1 in February 1979 along with
1230 radiative transfer simulations from 4 different reanalyses, clear scenes only over ocean [Data set]. Zenodo.
1231 https://doi.org/10.5281/zenodo.7912742
1232 Privette, J. L., Wenying, S., Schulz, J., & Merchant, C. J. (2023). A Definitions Taxonomy for Satellite Climate
1233 Data Records and Time Series Data Sets (Vol. Poster Session 1-Other Topics on Climate Variability and
1234 Change (Posters)). Presented at the American Meteorologial Society - 103rd AMS Annual Meeting,
1235 Denver, CO. Retrieved from https://ams.confex.com/ams/103ANNUAL/meetingapp.cgi/Program/1620
1236 Quast, R., Giering, R., Govaerts, Y., Rüthrich, F., & Roebeling, R. (2019). Climate Data Records from Meteosat
1237 First Generation Part II: Retrieval of the In-Flight Visible Spectral Response. *Remote Sensing*, *11*(5), 480.
1238 https://doi.org/10.3390/rs11050480
1239 Rodgers, C. D., & Walshaw, C. D. (1963). Polynomial approximations to radiative functions. *Quarterly Journal of*
1240 *the Royal Meteorological Society*, *89*(381), 422–423. https://doi.org/10.1002/qj.49708938116
1241 Rodgers, Clive D. (1990). Characterization and error analysis of profiles retrieved from remote sounding
1242 measurements. *Journal of Geophysical Research*, *95*(D5), 5587. https://doi.org/10.1029/JD095iD05p05587
1243 Ruti, P. M., Tarasova, O., Keller, J. H., Carmichael, G., Hov, Ø., Jones, S. C., et al. (2020). Advancing Research for
1244 Seamless Earth System Prediction. *Bulletin of the American Meteorological Society*, *101*(1), E23–E35.
1245 https://doi.org/10.1175/BAMS-D-17-0302.1

1246 Saunders, R., Hocking, J., Turner, E., Rayer, P., Rundle, D., Brunel, P., et al. (2018). An update on the RTTOV fast
1247 radiative transfer model (currently at version 12). *Geoscientific Model Development*, *11*(7), 2717–2737.
1248 https://doi.org/10.5194/gmd-11-2717-2018
1249 Schipper, E. L. F. (2020). Maladaptation: When Adaptation to Climate Change Goes Very Wrong. *One Earth*, *3*(4),
1250 409–414. https://doi.org/10.1016/j.oneear.2020.09.014
1251 Schweiger, A. K., & Laliberté, E. (2022). Plant beta-diversity across biomes captured by imaging spectroscopy.
1252 *Nature Communications*, *13*(1), 2767. https://doi.org/10.1038/s41467-022-30369-6
1253 Shahabadi, M. B., Aparicio, J. M., & Garand, L. (2018). Impact of Slant-Path Radiative Transfer in the Simulation
1254 and Assimilation of Satellite Radiances in Environment Canada's Weather Forecast System. *Monthly*
1255 *Weather Review*, *146*(12), 4357–4372. https://doi.org/10.1175/MWR-D-18-0126.1
1256 Stenchikov, G. L., Kirchner, I., Robock, A., Graf, H.-F., Antuña, J. C., Grainger, R. G., et al. (1998). Radiative
1257 forcing from the 1991 Mount Pinatubo volcanic eruption. *Journal of Geophysical Research: Atmospheres*,
1258 *103*(D12), 13837–13857. https://doi.org/10.1029/98JD00693
1259 Stephens, G. L. (1994). *Remote sensing of the lower atmosphere: an introduction*. New York: Oxford University
1260 Press.
1261 Stöckli, R., Bojanowski, J. S., John, V. O., Duguay-Tetzlaff, A., Bourgeois, Q., Schulz, J., & Hollmann, R. (2019).
1262 Cloud Detection with Historical Geostationary Satellite Sensors for Climate Applications. *Remote Sensing*,
1263 *11*(9), 1052. https://doi.org/10.3390/rs11091052
1264 Swales, D. J., Pincus, R., & Bodas-Salcedo, A. (2018). The Cloud Feedback Model Intercomparison Project
1265 Observational Simulator Package: Version 2. *Geoscientific Model Development*, *11*(1), 77–81.
1266 https://doi.org/10.5194/gmd-11-77-2018
1267 Théodore, B., Coppens, D., Doehler, W., Damiano, A., Oertel, D., Klaes, D., et al. (2015). A glimpse into the past:
1268 rescuing hyperspectral SI-1 data from Meteor-28 and 29. Presented at the EUMETSAT Meteorological
1269 Satellite Conference, Toulouse, France: EUMETSAT.
1270 Thorpe, A., & Rogers, D. (2018). The Future of the Global Weather Enterprise: Opportunities and Risks. *Bulletin of*
1271 *the American Meteorological Society*, *99*(10), 2003–2008. https://doi.org/10.1175/BAMS-D-17-0194.1

1272 Watkin, S. C. (2003). The application of AVHRR data for the detection of volcanic ash in a Volcanic Ash Advisory
1273 Centre: Application of AVHRR data in volcanic ash detection. *Meteorological Applications*, *10*(4), 301–
1274 311. https://doi.org/10.1017/S1350482703001063
1275 WCC-3. (2009a). Conference Declaration. Geneva, Switzerland. Retrieved from
1276 https://gfcs.wmo.int/sites/default/files/WCC3_declaration_en.pdf
1277 WCC-3. (2009b). Conference Statement. Geneva, Switzerland. Retrieved from
1278 https://gfcs.wmo.int/sites/default/files/WCC-3_Statement_07-09-09 mods.pdf
1279 Wickham, H. (2011). The Split-Apply-Combine Strategy for Data Analysis. *Journal of Statistical Software*, *40*(1).
1280 https://doi.org/10.18637/jss.v040.i01
1281 World Meteorological Organization (WMO). (2018). *Step-by-step Guidelines for Establishing a National*
1282 *Framework for Climate Services*. Geneva, Switzerland: WMO. Retrieved from
1283 https://library.wmo.int/doc_num.php?explnum_id=4335
1284 World Meteorological Organization (WMO), & European Commission. (2015). *Satellites for Climate Services: case*
1285 *studies for establishing an architecture for climate monitoring from space*. Geneva: WMO. Retrieved from
1286 https://library.wmo.int/index.php?lvl=notice_display&id=18883
1287 World Meteorological Organization (WMO), United Nations Educational Scientific and Cultural Organization
1288 (UNESCO), Intergovernmental Oceanographic Commission (IOC), United Nations Environment
1289 Programme (UNEP), & International Science Council (ISC). (2022). *The 2022 GCOS Implementation*
1290 *Plan*. Geneva, Switzerland: WMO. Retrieved from
1291 https://library.wmo.int/index.php?lvl=notice_display&id=22134
1292